Monitoring of large-scale CO_2 injection using CSEM, gravimetric, and seismic AVO data

Svenn Tveit[1] **and Trond Mannseth**[1]

[1]NORCE Norwegian Research Centre AS

Corresponding author: Svenn Tveit, svtv@norceresearch.no

Abstract

A sequential inversion methodology for combining geophysical data types of different resolutions is developed and applied to monitoring of large-scale CO_2 injection. The methodology is a two-step approach within the Bayesian framework where lower resolution data are inverted first, and subsequently used in the generation of the prior model for inversion of the higher resolution data. For the application of CO_2 monitoring, the first step is done with either controlled-source electromagnetic (CSEM) or gravimetric data, while the second step is done with seismic amplitude-versus-offset (AVO) data. The Bayesian inverse problems are solved by sampling the posterior probability distributions using either the ensemble Kalman filter or ensemble smoother with multiple data assimilation. A carefully designed parameterization is used to represent the unknown geophysical parameters: electric conductivity, density, and seismic velocity. The parameterization is well suited for identification of CO_2 plume location and variation of geophysical parameters within the regions corresponding to inside and outside of the plume. The inversion methodology is applied to a synthetic monitoring test case where geophysical data are made from fluid-flow simulation of large-scale CO_2 sequestration in the Skade formation in the North Sea. The numerical experiments show that seismic AVO inversion results are improved with the sequential inversion methodology using prior information from either CSEM or gravimetric inversion.

1 Introduction

This chapter is an extended version of Tveit et al. (2020). In particular, we give a broader presentation of the controlled-source electromagnetic (CSEM) experiment. For a broader presentation of the gravimetric method we refer to the chapter by Appriou & Bonneville (2021). The seismic method is presented in several chapters, e.g., Mur et al. (2021). While ensemble methods are operational in weather forecasting and industry standard in petroleum-reservoir history matching, they are much less frequently seen in publications concerned with geophysical inverse problems, like modeling of CO_2 monitoring. A broader introduction to ensemble methods than in Tveit et al. (2020) is therefore given here. The parameterization of the unknown parameter functions (i.e., seismic velocity, electric conductivity, density) applied in Tveit et al. (2020) is not standard in geophysical inversion, and perhaps, somewhat 'mathematical'. A broader introduction to parameterization is therefore given here as well. In addition, we explain certain con-

cepts more thoroughly than what the standard journal-paper format allows for. We have chosen to keep the appendices in Tveit et al. (2020) also here for the benefit of readers interested in all details of the inversion methodology.

Storing CO_2 in large, saline aquifers is considered one of the remedies for greenhouse-gas emission. Cost-efficient CO_2 sequestration in large aquifers with an aim to store a large amount of CO_2 over a restricted period of time will likely involve high injection rate spread over few injection wells. The combination of high injection rate and few injection wells can lead to hazardous pressure build-ups. If pressure develops over certain thresholds, situations like, e.g., near-well fracturing and fault reactivation can occur, with possibly severe consequences. To be able to detect areas with potential hazardous over-pressure, especially far from the wells, periodical geophysical monitoring surveys have to be conducted. Geophysical monitoring is also important for verifying CO_2plume placement and fluid-flow simulations, and detecting leakage to the surface.

1.1 Controlled-source electromagnetics

A typical CSEM survey consists of first deploying receivers on the seafloor which contain AC-coupled electric field sensors and induction-coil magnetometers (Constable, 2013). The seafloor receivers are capable of recording all components of the electric and magnetic fields, although it is most common to use the electric field in inversion. After receiver deployment, a 100–300 m horizontal electric dipole (HED) source is towed near the seafloor (25–100 m above) passing a time-varying current commonly with a strength of 500–1000 A. Vertical source geometry and magnetic dipoles exist, but HED is preferred due to electric currents being easier to generate and it produces both horizontal and vertical fields (Nabighian, 1991). It is by far most common to process the recorded electromagnetic (EM) signals in the frequency domain. Thus the transmitted signal from the source is mostly a binary waveform in the range 0.1–10 Hz with the possibility of emphasizing key harmonics. Alternatively, for time-domain processing the source signal is a step on/off current which broadcasts over a wide frequency range. Although the underlying physics are the same, processing time- or frequency-domain signals have different benefits depending on the application. Note that, even though seafloor-deployed receivers are most common, towed-source and receiver setups have been extensively developed in recent years, see, e.g., Constable et al. (2016).

The EM signal transmitted from the source is diffusive in nature, due to the low frequencies, and is modified by the electric conductivity of the propagated media. There are several mechanisms at work when EM signals travel through media with different conductivity, and the complex interplay between these mechanisms determines the responses measured in the receivers. First, we have *geometric spreading* where the EM signals are reduced by a factor proportional to the cubic distance traveled. This is generally the dominating mechanism near the source where the EM signal is strong. Second, we have *attenuation* where EM signals decay with an exponential factor due to their inductive nature. This is the dominating mechanism away from the source. Attenuation is typically measured in terms of skin depth, which indicates the distance required for an EM signal to be reduced by a factor $1/e$ ($\approx 37\%$), and is a function of frequency and conductivity. For frequencies used in CSEM the skin depth is short in conductive media such as seawater, which explains why a source has to be towed close to the seafloor.

When EM signals cross the boundary between two media with different conductivity, two mechanisms are important: the *galvanic* and *inductive effects*. The galvanic effect is a jump in the electric field due to continuity of normal current density. If the conductivity decreases across the boundary, the electric field must increase according to Ohm's law. Furthermore, in less conductive media, such as CO_2- or hydrocarbon-bearing bodies, the attenuation is significantly less, resulting in EM signals propagating in the body as 'guided waves' (Key, 2016; Weidelt, 2007). In sum, the galvanic effect has the potential to produce strong responses as the EM signals radiate from the less conductive body back to the seafloor receivers. The inductive effect is a change in current density due to continuity of the tangential electric field across the boundary. The change in current density induces a magnetic field, according to Ampere's law, that works against the electric field. Compared to the galvanic effect, the responses from EM signals produced by the inductive effect are significantly smaller. Lastly, we note that since air is non-conductive, the signals traveling there do not attenuate, thus strong EM fields (called airwaves) radiate from the air-sea boundary. The source-receiver offset where the airwave dominates over the galvanic and induced effects from the subsurface depends on the sea depth (Um & Alumbaugh, 2007).

The source-receiver geometry is important to produce galvanic and inductive effects such that a target in the subsurface is detected. When the source and receivers are inline, largely galvanic effects will be produced in the subsurface, while receivers broad-

side to the source record largely inductive effects. For economic reasons and the observation that galvanic effects produce stronger responses, it seems natural to only perform surveys with inline source-receiver geometries. However, as demonstrated in Eidesmo et al. (2002) and Constable (2010), ambiguous results may occur from strong galvanic effects regarding the thickness of the target, which is not present with the inductive effects. Thus, it is recommended to also record with broadside receivers either by towing the source over a line of receivers at different angles, or deploying a 2D array of receivers.

The conductivity of CO_2-filled porous media is in the range of 0.01–0.02 S/m, depending on CO_2 saturation. With the surrounding brine-filled porous media being mostly around 1 S/m, the conductivity contrast is significant enough to produce strong EM responses. Thus CSEM is a suitable method for monitoring CO_2 sequestration, which have been demonstrated in feasibility studies (Lien & Mannseth, 2008; Orange et al., 2009; Bhuyian et al., 2012; Park et al., 2017). Moreover, the studies generally show that the sensitivity to lateral variation of the target is high, which fits well our description of less conductive targets acting as 'waveguides'. On the contrary, the sensitivity to varying thickness of the target is lower. Furthermore, Bhuyian et al. (2012) studied various CO_2 sequestration scenarios, and showed that CSEM responses were sensitive to different CO_2-plume geometries and saturation values, including the ability to detect shallow CO_2 leakage using a range of frequencies. Lastly, there have been studies on the spatial resolution of the CSEM method, that is, how well a given structure is resolved from the data; see Key (2012) and references therein. In general, due to the low-frequency signals, it is anticipated than CSEM data will have coarser spatial resolution than seismic data.

1.2 Seismics and gravimetrics

The most widely used geophysical monitoring method is the seismic method. Being a mature field of science, a wealth of inversion (and imaging) techniques exist within the seismic method; from full-waveform inversion, which has become popular in recent years, to various approximation methods, such as ray-tracing. Here, we apply the common approximation method amplitude versus offset (AVO), see, e.g., Chopra & Castagna (2014), where elastic parameters are estimated from seismic reflection coefficients. Seismic time-lapse signals are sensitive to changes in subsurface elastic properties, where changes due to contrasts in both saturation and pressure are important for CO_2 monitoring. Discrimination between saturation and pressure effects is discussed, e.g., in Tura & Lum-

ley (1999); Landrø (2001); Trani et al. (2011); Davolio et al. (2012); Grude et al. (2013); Longxiao et al. (2016); Souza et al. (2017). Obtaining reliable saturation and pressure estimates from AVO data can be difficult, due to data and modeling errors, poor conditioning of the linearized AVO system, and significant uncertainties in the petroelastic model. To increase the reliability of inversion results, combining seismic data with information from complementary geophysical data types is an option. The complementary data types considered in this chapter are CSEM and gravimetric data.

Gravimetric methods have been used in many monitoring case studies, e.g., reservoir production monitoring, see, e.g., Vatshelle et al. (2017); Zumberge et al. (2008); Hare et al. (2008). The measured gravitational field in monitoring studies is sensitive to changes in density. The CO_2 density is (in most cases) less than the brine density, and the density change resulting from displacing brine by CO_2 is significant enough to produce detectable gravity signals. In addition to density changes due to different fluid content in the pores, the fluid densities are dependent on pressure (and temperature). Hence, it is possible to monitor pressure and saturation effects with gravity data, although pressure effects on density are often weak. The spatial resolution of gravity data is lower than that of seismic data. The cost of gravity measurements is, however, lower than those of seismic and CSEM measurements. Several studies have concluded that gravity data provide valuable information for CO_2 monitoring, both as stand-alone measurements and as a supplement to other geophysical methods (Gasperikova & Hoversten, 2008; Alnes et al., 2011; Ishido et al., 2011; Landrø & Zumberge, 2017). We note that reliable gravimetric measurements are dependent on accurate subsidence/uplift mapping at receiver locations, to correctly account for the distance to Earth's center in the data processing.

1.3 Joint utilization of disparate data types

Disparate geophysical data types have different associated strengths and weaknesses, and separate inversion of such data types will typically lead to inconsistent images of the same target. Since the data types contain complementary information about the target, there is, however, a potential for obtaining an improved image by combining them. Unfortunately, combining complementary geophysical data types is not a straightforward process. Scale issues, such as differences in resolution, is one obstacle that must be overcome. Proper uncertainty specification for the data types presents another difficulty. This is perhaps particularly pronounced for seismic data, since they have typically gone through

a number of processing steps before inversion starts. Erroneous specification of uncertainty for a data type will directly influence the relative weight put on that data type in the inversion.

Many of the joint-inversion techniques that have been suggested in the literature are based on the assumption that the data types are linked through petrophysical or structural relationships. Use of petrophysical relationships between saturation and pressure and elastic and electric properties allows for direct estimation of time-lapse saturation and pressure changes. Although petrophysical relationships are built from an underlying theory, they contain several unknown parameters and therefore require calibration to experimental data. Since laboratory samples can never fully represent the true subsurface, a modeling error is introduced when performing joint inversion using petrophysical relationships. Examples of joint-inversion techniques using petrophysical relationships can be found, e.g., in Hoversten et al. (2006); Moorkamp et al. (2011); Abubakar et al. (2012); Chen & Hoversten (2012).

Alternatively, joint-inversion techniques based on assumed underlying structural relationships between selected functions of time-lapse saturation and pressure changes in the different geophysical regimes can be used. Such techniques estimate these functions (e.g., time-lapse changes in seismic velocity and electric conductivity) in the inversion, while the corresponding saturation and pressure changes can be found from petrophysical relationships after the geophysical inversion, if desired. The cross-gradient approach, introduced in Gallardo & Meju (2003), is perhaps most common among such joint-inversion techniques. With this approach, it is basically enforced during the inversion that large spatial variations in seismic velocity and electric conductivity should only occur along the same directions. Examples of structural joint-inversion techniques can be found in Haber & Oldenburg (1997); De Stefano et al. (2011); Gallardo & Meju (2011); Lien (2013).

While the joint-inversion techniques described above aim to utilize complementary data types in a single inversion process, so-called cooperative inversion techniques (Lines et al., 1988) aim to invert the data types in separate steps, with the resulting model from inversion of one data type acting as starting model or constraint for the subsequent inversion of another data type. Examples of cooperative inversion techniques can be found in Tveit et al. (2015a,b), where interpreted seismic inversion results are used as struc-

tural prior information for CSEM inversion, and in Hu et al. (2009); De Stefano et al. (2011); Takougang et al. (2015), where inversion of each data type is done in sequence and, in some cases, iterated. Exchanging information between geophysical models in the disparate inversion sequences can be challenging, especially if the spatial resolutions of the data types are different. In Um et al. (2014), seismic velocity and electric resistivity models were coupled through exchange of structural information, but that required an extra inversion step between the (iterated) inversion sequences.

Our inversion strategy belongs within the Bayesian framework. Data and unknown parameters are considered as random variables, and the solution to the inverse problem is the posterior probability density function (PDF) for the unknown parameters. From the posterior PDF a best-estimate geophysical model (the mean) with associated uncertainty and correlations (the covariance) can be extracted, if desired. Bayes' rule for PDFs states that the posterior PDF is proportional to the product of the prior PDF for the unknown parameters and the PDF for the observed data given the parameters. The prior PDF can be formed using all types of information except the observed data used when calculating the posterior. A geologist opinion is a prime example of information that can be suitable when building the prior PDF. It is, however, also possible to use information obtained from one data type in the construction of a prior model for inversion of another data type that is independent of the first one (sequential Bayesian inversion).

To use different geophysical data types jointly, we follow ideas from cooperative inversion, and further develop an inversion strategy introduced in Tveit et al. (2016). We suggest a sequential approach where data with lower spatial resolution are inverted first, and subsequently, the results are applied in the construction of the prior model for the inversion of data with higher resolution. As discussed above, both CSEM and gravimetric data have lower spatial resolution than seismic AVO data. Thus, either CSEM or gravimetric inversion will be performed in the first step, before the seismic AVO inversion in the second step. The construction of the prior model for the seismic inversion is facilitated by using the same type of parameterization for the unknown functions in the CSEM, gravity, and seismic inversions.

1.4 Parameterization

Basically, parameterization refers to selection of the variables used to formulate the problem, and selecting a suitable parameterization can make the problem considerably simpler to solve. An obvious example is use of polar coordinates in analytic integration over a 2-D region with circular boundaries. For an inverse problem, parameterization refers to selection of a mathematical representation for the unknown function controlled by a set of parameters that are to be estimated. The conceptually most simple parameterization is perhaps to represent the unknown function by its values on the forward-simulator grid (pixel parameterization). We will apply a more advanced parameterization (see, e.g., Berre et al., 2011; Tveit et al., 2015b) based on the level-set framework that, contrary to the pixel parameterization, facilitates representation of region boundaries without a priori restrictions on their shapes. It is therefore well suited to represent the boundaries of the images of a large-scale CO_2 plume in the respective geophysical domains, that is, in the electric conductivity, density, and seismic velocity. It is expected that these properties will be slowly varying both within the region corresponding to the plume and outside that region, while the variation can be abrupt when crossing the region boundary. The applied parameterization is able to handle this type of variation using a relatively small number of parameters.

1.5 Sampling the posterior distribution

For the cases considered here (and for most other cases), a complete characterization of the posterior PDF is only possible by using sampling techniques. A sample from a PDF for a random variable is a set of correctly generated realizations of that random variable. The term 'correctly generated' means that if the sample size is sufficiently large, all properties of the PDF can be accurately estimated from the sample. Markov chain Monte Carlo (MCMC) methods can sample correctly from the posterior PDF, but require a huge number of forward-model runs for a sufficient description of the posterior PDF. For application of MCMC methods to geophysical problems, see, e.g., Bodin & Sambridge (2009); Buland & Kolbjørnsen (2012); Ray & Key (2012); Gunning & Glinsky (2004).

MCMC methods have an extremely high computational cost for realistically-sized problems. To reduce computational costs, two ensemble-based Bayesian methods, the ensemble Kalman filter (EnKF) (Evensen, 1994) and the ensemble smoother with mul-

tiple data assimilation (ES-MDA) (Emerick & Reynolds, 2013), which require only a moderate number of forward-model runs, will be applied here. These methods have an underlying Gaussian assumption on the involved PDFs, and can therefore be shown to sample correctly from the posterior PDF only in the case where the prior PDF is Gaussian and the forward model is linear, in the limit of an infinite ensemble size. They have, however, been shown to sample approximately correct in many scientific fields where the forward models are nonlinear, see, e.g., Evensen (2009) and Aanonsen et al. (2009), and references therein. Ensemble-based Baysian methods have been used for inversion of CSEM data (Tveit et al., 2015a) and inversion of seismic data (Liu & Grana, 2018; Gineste & Eidsvik, 2015, 2017; Thurin et al., 2017).

1.6 Skade formation

The inversion methodology will be applied to a synthetic CO_2 monitoring test case where the geophysical reference ('true') models are made based on fluid-flow simulations of large-scale CO_2 sequestration with three injection wells in the Skade formation (Elenius et al., 2018). The Skade formation is considered a potential candidate for storing large amount of CO_2 in the North Sea (Halland et al., 2014). In the test case, we consider a 2D cross section through one of the injection wells. Thus, the test case serves as a feasibility study to asses the effectiveness of long-term monitoring of CO_2 sequestration in the formation.

1.7 Outline

The chapter is organized as follows: in Section 2, the forward models for CSEM, gravimetry, and seismic methods are presented. Section 3 describes the inverse problem and consists of three main parts: the parameterization is described in Section 3.1 followed by the ensemble-based, Bayesian methods in Section 3.2, and lastly sequential utilization of CSEM, gravimetric, and seismic data is discussed in Section 3.3. The numerical setup and results from the test case will be presented in Section 4. We end with some concluding remarks in Section 5.

2 Forward Models

The rock physics model, converting reservoir saturation and pressure to geophysical variables, is described in Section 4.1. The three geophysical methods used in this chapter — CSEM, seismic, and gravimetry — are simulated using three separate forward solvers. Common for all three forward models is that the computational domain is 2D, denoted $\Gamma \in \mathbb{R}^2$. In the following, let $\mathbf{x} = (x, z)^T$ denote an arbitrary position vector, and let N_g be the number of grid cells when Γ is discretized.

2.1 CSEM

The governing equations for the EM signals are the Maxwell's equations. Here, we focus on the frequency-domain formulation in the quasi-static approximation,

$$\nabla \times \mathbf{e} = i\omega\mu\mathbf{h}, \tag{1}$$

$$\nabla \times \mathbf{h} - \sigma\mathbf{e} = \mathbf{j}^e, \tag{2}$$

$$\nabla \cdot \mu\mathbf{h} = 0, \tag{3}$$

$$\nabla \cdot \epsilon\mathbf{e} = 0, \tag{4}$$

where $\mathbf{e}$ is the electric field, $\mathbf{h} = \mu^{-1}\mathbf{b}$ is an auxillary vector to the magnetic field $\mathbf{b}$, and $\mathbf{j}^e$ is the source current density. Furthermore, μ denotes the magnetic permeability, ϵ denotes electric permittivity, and σ denotes the electric conductivity. The harmonic time convention used is $\exp(-i\omega t)$, where ω denotes the angular frequency and $i = \sqrt{-1}$. With the quasi-static approximation, we neglect time-varying currents (also called displacement currents) in Ampere's law (2), since their contribution in low-frequency signals is small. Moreover, we have assumed that no free electric charges are present.

Maxwell's equations are first-order, coupled partial differential equations (PDEs) that are often used in modeling CSEM responses. In many modeling approaches, however, it is more common to decouple the equations by simple mathematical manipulations. Eliminating $\mathbf{h}$ from (1)–(4) leads to,

$$\nabla \times \left(\mu^{-1}\nabla \times \mathbf{e}\right) - i\omega\sigma\mathbf{e} = i\omega\mathbf{j}^e. \tag{5}$$

From (5) we see that the price for decoupling Maxwell's equations is a second-order PDE. Furthermore, we can see from (5) that it resembles classical diffusion equations, which is a consequence of the quasi-static approximation and is why EM signals are diffusive in nature (Løseth et al., 2006).

An alternative formulation of (5) can be made using scalar and vector potentials. The approach applies Helmholtz decomposition to the electric field, reducing it to the sum of a curl-free (i.e., a scalar potential) and a divergence-free (i.e., a vector potential) vector field. The decomposition splits the physics causing the electric field into two distinct sources, thus providing better handling of these sources in the modeling. The price paid is representing the three electric field components with four unknowns (three vector field components and one scalar), and thus requiring so-called gauge transformations to get a closed-form system of equations (see, e.g., Aruliah et al., 2001).

Most commonly, three approaches are used to solve the first- or second-order (with or without vector-scalar potentials) Maxwell's equations: integral equation, finite difference (including finite volume), and finite element approaches.

With the integral equation approach, the conductivity is split into background and anomalous (e.g., CO_2-bearing bodies) parts, $\sigma = \sigma^b + \sigma^a$, and the corresponding electric field is split in a similar manner, $\mathbf{e} = \mathbf{e}^b + \mathbf{e}^a$. The details for deriving the integral equations can be found, e.g., in Hohmann (1975), but in broad strokes it involves inserting the split electric field and conductivity into Maxwell's equations, multiplying with a dyadic Green's function, $\mathbf{G}(\mathbf{x}, \mathbf{x}')$, and integrating. The dyadic Green's function is essentially the electric field at $\mathbf{x}$ due to a unit current density at $\mathbf{x}'$, and can be calculated analytically for simple geometries, e.g., layered subsurface (see, e.g., Wannamaker et al., 1984), or numerically (see, e.g., Jakobsen & Tveit, 2018). The resulting equations are

$$\mathbf{e}^b(\mathbf{x}) = \int_Q \mathbf{G}(\mathbf{x}, \mathbf{x}')\mathbf{j}(\mathbf{x}')\mathrm{d}\mathbf{x}', \tag{6}$$

$$\mathbf{e}^a(\mathbf{x}) = \int_D \mathbf{G}(\mathbf{x}, \mathbf{x}')\sigma^a(\mathbf{x}')[\mathbf{e}^a(\mathbf{x}') + \mathbf{e}^b(\mathbf{x}')]\mathrm{d}\mathbf{x}', \tag{7}$$

where $\mathbf{j}$ denotes source currents, Q denotes the region containing source currents, and D denotes the region where σ^a is nonzero. The computationally intensive part is calculating $\mathbf{e}^a$ inside D, since discretization of (7) then results in a linear system with a dense system matrix. The upshot, however, is that D is typically much smaller than the region of interest, leading to a system matrix that, although dense, is not too large for computations.

With a traditional finite difference approach, the procedure is: discretize σ on a structured, rectangular grid; approximate Maxwell's equations by finite differences; and

solve the resulting linear system involving a large sparse band matrix. The major advantages with such an approach are the simplicity of the implementation and computational efficiency for problems with simplistic geometry, while the drawback is handling features at different scales, from source and receivers at order of meters to geological formations at the order of kilometers. For first-order Maxwell's equations, the electric and magnetic fields are typically represented on staggered grids following Yee (1966).

The solution procedure for a typical finite-element approach involves the following steps: discretize σ on an unstructured grid (e.g., with triangular elements); derive the governing equations for one element and assemble all elements in Γ; and solve the resulting sparse linear system. The major advantage with finite element approaches is the ability to conform the unstructured grid to complex model features, while the drawbacks are the involved procedure deriving the element equations and the special care required to solve the linear system involving a large sparse unstructured matrix.

In Section 4, the solution to (5) will be calculated using a 2.5D finite element approach, implemented in the MARE2DEM software (see Key, 2016; Key & Ovall, 2011, for extensive description of the simulator). Note that 2.5D refers to the quite popular approach of finding 3D vector fields ($\mathbf{e}$ or $\mathbf{h}$) by splitting the governing equations into sequences of 2D problems using Fourier transformation (Key, 2016). Finally, the computational domain, Γ, is discretized into N_g triangular elements using Triangle (Shewchuk, 1996).

2.2 Gravimetry

The gravity field, $\mathbf{g}$, must satisfy the following equations

$$\nabla \cdot \mathbf{g} = -4\pi G\rho, \quad \nabla \times \mathbf{g} = 0, \tag{8}$$

where G denotes the universal gravitational constant and ρ denotes the density. The gravimetric data measured at a site are vertical gravity fields, g_z, and contain everything that influences the gravitational field at the receiver locations. To remove the influences on the measurements from known but unwanted sources, the data are processed such that the remaining data (called gravity anomaly) are only due to an anomalous density, $\Delta\rho$, in the subsurface. The gravity anomaly for g_z is denoted Δg_z, and the general solution

of (8) for Δg_z is given as

$$\Delta g_z(\mathbf{x}) = 2G \int_\Gamma \Delta\rho(\mathbf{x}') \frac{z' - z}{\|\mathbf{x}' - \mathbf{x}\|^2} \mathrm{d}x' \mathrm{d}z'. \tag{9}$$

To solve (9), the analytical approach given in Talwani et al. (1959) is used, where Γ is discretized into N_g triangular elements with Triangle. It is assumed that $\Delta\rho$ is constant for each element.

2.3 Seismic AVO

In seismics, elastic waves are produced from a controlled source, and reflected and rarefracted waves are subsequently recorded by hydrophones offshore and geophones onshore. The main type of elastic waves affecting the recorded responses are primary, or pressure, (P) waves and secondary, or shear, (S) waves. P waves travel by compression of the media, while S waves are transverse, i.e., the movement is perpendicular to the direction of propagation. In reflection seismology methods, like AVO, we are only interested describing how P- and S waves are reflected and transmitted at a rock boundary. Specifically, AVO focuses on the relationship between reflection and transmission coefficients and the incident angle (or source-receiver offset), which is generally described by the Zoeppritz equations. Unfortunately, these equations are tedious to evaluate numerically, and often a linear approximation is used instead. Here, we follow an approach common in AVO and use incident and reflected P waves (R_{pp}) as data. To model R_{pp}, we use the linear approximation given in Aki & Richards (1980),

$$\begin{aligned} R_{pp} = &\frac{1}{2\cos^2\theta} \frac{\Delta V_p}{\bar{V}_p} - 4\frac{\bar{V}_s^{\,2}}{\bar{V}_p^2} \sin^2\theta \frac{\Delta V_s}{\bar{V}_s} \\ &+ \frac{1}{2}\left(1 - 4\frac{\bar{V}_s^{\,2}}{\bar{V}_p^2}\sin^2\theta\right)\frac{\Delta\rho}{\bar{\rho}}. \end{aligned} \tag{10}$$

V_p and V_s denote the P- and S-wave velocities, θ denotes the incident (or reflection) angle, and the overbar denotes average velocity over the reflecting surface. Note that the linear approximation (10) describes the reflection coefficient from one reflecting surface and one θ, and is only valid for weak velocity contrasts and θ significantly below the critical angle. To expand (10) for use with multiple θ and reflecting surfaces, we follow the description in Buland & Omre (2003, Appendix B). Note that, it is assumed that effects such as geometrical spreading, multiples, and absorption have been removed or corrected for in a (pre-)processing step, and it is also assumed that deconvolution and time-depth conversion have been performed. Furthermore, it is assumed that data recorded as a func-

tion of source-receiver offsets have been transformed to be function of incident angles, θ. (The transformation can be done with, e.g., ray-tracing or approximate offset-angle formulas.)

3 Inverse problem

We consider the sequential inversion strategy where electromagnetic or gravimetric data is inverted first, and utilize results from this inversion to construct a prior model for the inversion of seismic data. Several inverse sub problems, involving different physical quantities, will therefore be considered: inversion of seismic data to seismic velocity; electromagnetic data to electric conductivity, and; gravimetric data to density. Major components of the inversion methodologies applied to solve the different sub problems will, however, be identical. To keep the description of these common features of the methodology concise, we introduce a common notation. Let $\mathbf{d} \in \mathbb{R}^{N_d}$ denote measured data, $f(\mathbf{x}) \in \mathcal{F}$ the unknown function to be estimated, and $\mathbf{g}(f) \in \mathbb{R}^{N_d}$ the forward-model output. With frequency-domain CSEM, data will be complex. In that case, $\mathbf{d}$ and $\mathbf{g}$ will be augmented vectors containing real and imaginary parts of the complex data and forward-model output, respectively. To solve the associated inverse problem, that is, to estimate $f(\mathbf{x})$ from $\mathbf{d}$ and additional available information, we use an ensemble-based Bayesian method in conjunction with a carefully designed parameterization, $q(\mathbf{x};\mathbf{m}) \in \mathcal{Q}$, of $f(\mathbf{x})$, where $\mathbf{m} \in \mathbb{R}^{N_m}$ denotes the unknown parameter vector and $\mathcal{Q} \subset \mathcal{F}$. A description of how results from the different inverse sub problems are combined, and a reasoning behind the way the data types are utilized together in the sequential strategy, are given in Section 3.3. Results obtained with this strategy will be compared with those obtained by direct inversion of seismic data in Section 4. Note also that V_s and ρ are fixed at their true values in all seismic inversions.

3.1 Parameterization

The vast majority of papers concerned with solving inverse problems numerically parameterize the unknown function by a constant value in each forward-model grid cell (pixel parameterization). For inverse problems where the unknown function is expected to possess significant grid-cell-scale variations, using pixel parameterization makes perfect sense. For other types of inverse problems, using other types of parameterizations

might be advantageous. The point is to carefully consider the problem at hand before selecting which type of parameterization to apply.

Except perhaps in the immediate vicinity of injection wells, significant pressure variations on the grid-cell scale will not occur. Typically, there will not be significant grid-cell-scale variations in saturation inside or outside a CO_2 plume, except in the vicinity of the plume boundary, and time-lapse changes of a CO_2 plume are primarily shape and volume changes. A suitable parameterization for estimation of time-lapse changes of a CO_2 plume should therefore be flexible with respect to what spatial shapes it can represent, and it should facilitate shape changes. On the other hand, it does not necessarily have to allow for significant spatial grid-cell-scale variations, except close to the plume boundary.

We will estimate time-lapse changes in functions of saturation and pressure, like density, seismic velocity and electric conductivity. These functions might experience spatial grid-cell-scale variations everywhere, since they are functions also of rock properties. Time-lapse changes in these functions are, however, not expected to possess such variations, since rock properties are considered to be constant in time. Hence, one may argue that the same type of parametrization that is suitable for estimation of time-lapse changes of a CO_2 plume itself is also suitable for our purposes.

We will describe a parameterization that meets the requirements outlined above. This parameterization is not standard, and we will therefore relate it to more standard parametrizations. We start by writing the pixel parameterization in a mathematical notation suitable for describing also the parameterization that we apply.

Let the inversion region, Ω, be the union of the members in a set of predetermined non-overlapping subdomains, $\{\Omega_j\}_{j=1}^{N_m}$, and let $\chi_j(\mathbf{x})$ denote the indicator function for Ω_j (i.e. $\chi_j = 1$ in Ω_j and zero elsewhere). One may then write $q(\mathbf{x};\mathbf{m})$ as a linear basis expansion

$$q(\mathbf{x};\mathbf{m}) = \sum_{j=1}^{N_m} m_j \chi_j(\mathbf{x}), \tag{11}$$

that is, a standard zonation with zones $\{\Omega_j\}_{j=1}^{N_m}$. Letting $N_m = N_g$ and letting Ω_j correspond to grid cell number j results in (11) being a pixel parameterization of f.

Since we can select zone boundaries as we please, a standard zonation is flexible with respect to what shapes it can represent. The zones are, however, fixed when solv-

ing the inverse problem while the values in each zone, the m_j's, are estimated. This is not satisfactory for our purposes, since shape changes are essential. In order to change zone boundaries, one may introduce dependencies on a set of control parameters in the basis functions, $\{\chi_j\}_{j=1}^{N_m}$. To this end, let the parameter vector consist of two sub vectors; $\mathbf{m}^T = (\mathbf{c}^T, \mathbf{a}^T)$, where $\mathbf{c} \in \mathbb{R}^{N_c}$, $\mathbf{a} \in \mathbb{R}^{N_a}$ and $N_c + N_a = N_m$, and write $q(\mathbf{x}; \mathbf{m})$ as a non-standard zonation with N_c zones,

$$q(\mathbf{x}; \mathbf{m}) = \sum_{j=1}^{N_c} c_j \chi_j(\mathbf{x}; \mathbf{a}). \tag{12}$$

The dependencies of the χ_js on $\mathbf{a}$ may be utilized to change the boundaries of the corresponding zones, while $\mathbf{c}$ now plays the role that $\mathbf{m}$ has in a standard zonation.

We will do shape estimation, and therefore parameterize f by what can be seen as an approximation to a particular type of non-standard zonation — the reduced, smoothed level-set representation. Details on the representation can be found in Tveit et al. (2015a,b), and references therein. For the convenience of the reader, we have summarized the representation in Appendix A. As is evident from this exposition, we will also apply an extended version of this type of parameterization by allowing the coefficients multiplying the basis functions to vary spatially. This extension is useful when inverting seismic AVO data, to allow for large-scale pressure variations in V_p. Note also that the reduced, smoothed level-set representation can easily be extended to 3D, following Berre et al. (2011).

3.2 Ensemble-based Bayesian inversion

The relation between the random variables $\mathbf{d}$ and $\mathbf{m}$ is

$$\mathbf{d} = \mathbf{g}(\mathbf{m}) + \epsilon_d, \tag{13}$$

where $\epsilon_d \in \mathbb{R}^{N_d}$ denotes the a realization of the measurement error vector, and $\mathbf{g}(q(\mathbf{x}; \mathbf{m}))$ has been written $\mathbf{g}(\mathbf{m})$ for convenience. Before any data have been applied, $\mathbf{m}$ follows the prior probability density function (PDF) $p(\mathbf{m})$, and for a given $\mathbf{m}$, $\mathbf{d}$ follows the conditional PDF $p(\mathbf{d}|\mathbf{m}) = p(\epsilon_d = \mathbf{d} - \mathbf{g}(\mathbf{m}))$, which we assume is a zero-mean Gaussian distribution with covariance matrix $\mathbf{C}_d$. Bayes' rule for PDFs then implies that the conditional PDF of $\mathbf{m}$ given $\mathbf{d}$ obeys

$$p(\mathbf{m}|\mathbf{d}) \propto p(\mathbf{d}|\mathbf{m}) p(\mathbf{m}). \tag{14}$$

The posterior PDF, $p(\mathbf{m}|\mathbf{d})$, describes the complete Bayesian solution to the inverse problem.

An analytical expression for $p(\mathbf{m}|\mathbf{d})$ is only feasible when $p(\mathbf{m})$ is Gaussian and $\mathbf{g}(\mathbf{m})$ is linear. Otherwise, $p(\mathbf{m}|\mathbf{d})$ must be characterized through sampling. Markov-chain Monte Carlo methods can sample correctly from $p(\mathbf{m}|\mathbf{d})$, but are prohibitively computationally expensive for realistic geophysical problems. In Sections 3.2.3 – 3.2.4 we describe the computationally feasible, approximate sampling methods for parameter estimation that are applied in this chapter; the ensemble smoother with multiple data assimilation (ES-MDA) (Emerick & Reynolds, 2013) and the ensemble Kalman filter (EnKF) (Evensen, 1994). For convenience of the reader, we will, however, first briefly describe the Kalman filter (Kalman, 1960) and the ensemble smoother (van Leeuwen & Evensen, 1996) in a parameter-estimation setting.

3.2.1 Kalman filter

Let $\mathbf{m}^0$ and $\mathbf{m}^1$ denote the prior and posterior model, respectively. If $p(\mathbf{m}^0)$ is Gaussian and $\mathbf{g}(\mathbf{m})$ is linear, that is, $\mathbf{g}(\mathbf{m}) = \mathbf{A}\mathbf{m}$, $p(\mathbf{m}^1|\mathbf{d})$ will be Gaussian. Its mean is expressed by the Kalman-filter equations (Jazwinski, 1970),

$$\mathbf{w} = \mathbf{A}\bar{\mathbf{m}}^0, \tag{15}$$

$$\mathbf{K} = \mathbf{C}_{m^0 w}\left(\mathbf{C}_w + \mathbf{C}_d\right)^{-1}, \tag{16}$$

$$\bar{\mathbf{m}}^1 = \bar{\mathbf{m}}^0 + \mathbf{K}\left(\mathbf{d} - \mathbf{w}\right), \tag{17}$$

where $\mathbf{K}$ denotes the Kalman gain, and $\bar{\mathbf{y}}$ and $\mathbf{C}_y$ denote the mean and auto covariance of $\mathbf{y}$, for any $\mathbf{y}$. Furthermore, $\mathbf{C}_{yz}$ denotes the cross covariance between $\mathbf{y}$ and $\mathbf{z}$, for any $\mathbf{y}$ and $\mathbf{z}$.

3.2.2 Ensemble smoother

If $p(\mathbf{m}^0)$ is not Gaussian and/or $\mathbf{g}(\mathbf{m})$ is nonlinear, $p(\mathbf{m}^1|\mathbf{d})$ must be characterized by sampling. With the ensemble smoother, (15)–(17) are applied to each member in the sample (ensemble member) and $\mathbf{C}_{m^0 w}$ and $\mathbf{C}_w$ in (16) are replaced by the empirical covariances, $\widetilde{\mathbf{C}}_{m^0 w}$ and $\widetilde{\mathbf{C}}_w$, calculated from the corresponding ensembles.

To be able to write the ensemble-smoother equations in a concise manner, let $\mathbf{M}$ and $\mathbf{D}$ denote the matrices holding the model ensemble members and data ensemble members as columns, respectively; $\mathbf{M} = (\mathbf{m}_1, \mathbf{m}_2, \ldots, \mathbf{m}_{N_e})$, $\mathbf{D} = (\mathbf{d}_1, \mathbf{d}_2, \ldots, \mathbf{d}_{N_e})$. Hence, $\mathbf{M}^0$ contains a sample from $p(\mathbf{m}^0)$ and $\mathbf{M}^1$ contains a sample from $p(\mathbf{m}^1|\mathbf{d})$. To gener-

ate $\mathbf{M}^0$, we use the Cholesky decomposition method described in Appendix B. The matrix $\mathbf{D}$ contains a sample from $\mathcal{N}(\mathbf{d}, \mathbf{C}_d)$, where $\mathcal{N}$ denotes the Gaussian distribution. Defining the matrices $\mathbf{G}(\mathbf{M}) = (\mathbf{g}(\mathbf{m}_1), \mathbf{g}(\mathbf{m}_2), \ldots, \mathbf{g}(\mathbf{m}_{N_e}))$ and $\mathbf{W} = (\mathbf{w}_1, \mathbf{w}_2, \ldots, \mathbf{w}_{N_e})$, the ensemble-smoother equations may be written as

$$\mathbf{W} = \mathbf{G}\left(\mathbf{M}^0\right), \tag{18}$$

$$\widetilde{\mathbf{K}} = \widetilde{\mathbf{C}}_{m^0 w}\left(\widetilde{\mathbf{C}}_w + \mathbf{C}_d\right)^{-1}, \tag{19}$$

$$\mathbf{M}^1 = \mathbf{M}^0 + \widetilde{\mathbf{K}}\left(\mathbf{D} - \mathbf{W}\right). \tag{20}$$

From $\mathbf{M}^1$, one may calculate approximations to the two first moments of $p(\mathbf{m}^1|\mathbf{d})$, $\bar{\mathbf{m}}^1$ and $\mathbf{C}_{m^1}$, empirically. The ensemble smoother thus provides a best estimate and a quantification of its uncertainty. The sample mean, $\widetilde{\mathbf{m}}^1$, can be obtained by inserting $\mathbf{m}^1$ for $\mathbf{y}$ in Appendix C, while the sample covariance, $\widetilde{\mathbf{C}}_{m^1}$, can be obtained by inserting $\mathbf{m}^1$ for $\mathbf{y}$ and $\mathbf{z}$.

3.2.3 Ensemble smoother with multiple data assimilation

When $\mathbf{g}(\mathbf{m})$ is nonlinear, iterations are generally required to obtain an accurate estimate for $\mathbf{m}$, while the ensemble smoother assimilates $\mathbf{d}$ in a single step. In an attempt to alleviate this problem with the ensemble smoother, the ES-MDA allows for $\mathbf{d}$ to be assimilated in N_u smaller steps in a statistically correct manner. To this end, a sequence of real positive scalars, $\eta_{1:N_u}$, is introduced, and it is required that $\sum_{u=1}^{N_u} \eta_u^{-1} = N_u$ (Emerick & Reynolds, 2013). The data-error covariance in cycle number u is inflated by η_u, that is, $\mathbf{D}^u$ contains a sample from $\mathcal{N}(\mathbf{d}, \eta_u \mathbf{C}_d)$, such that the estimate after completion of u cycles will depend on $\eta_{1:u}$.

To describe the ES-MDA in the ensemble-matrix notation introduced in Section 3.2.2, let $\mathbf{M}^u$ denote $\mathbf{M}$ after assimilation cycle number u has been completed, that is, $\mathbf{M}^u$ contains a sample from $p(\mathbf{m}^u|\mathbf{d}, \eta_{1:u})$. The ES-MDA equations for cycle number u may then be written as

$$\mathbf{W}^u = \mathbf{G}\left(\mathbf{M}^{u-1}\right), \tag{21}$$

$$\widetilde{\mathbf{K}}^u = \widetilde{\mathbf{C}}_{m^{u-1} w^u}\left(\widetilde{\mathbf{C}}_{w^u} + \eta_u \mathbf{C}_d\right)^{-1}, \tag{22}$$

$$\mathbf{M}^u = \mathbf{M}^{u-1} + \widetilde{\mathbf{K}}^u\left(\mathbf{D}^u - \mathbf{W}^u\right). \tag{23}$$

After cycle number N_u one obtains the final updated model ensemble $\mathbf{M}^{N_u}$, from which one may calculate empirical approximations to the two first moments of the posterior

PDF, $p(\mathbf{m}^{N_u}|\mathbf{d}, \eta_{1:N_u})$, in a similar mannner as described in the final paragraph of Section 3.2.2. Typical values for N_u are 4 – 8. Theoretical and practical procedures for choosing η_u can be found in Rafiee & Reynolds (2017).

3.2.4 Ensemble Kalman filter

While the ensemble smoother assimilates all data simultaneously in a single step and the ES-MDA assimilates all data simultaneously in a sequence of smaller steps, the EnKF is a sequential estimation methodology that assimilates part of the data in each assimilation cycle until all available data have been assimilated. It has been shown (Fossum & Mannseth, 2014a,b) that sequential estimation can be expected to outperform simultaneous estimation in a single step for weakly nonlinear problems.

To describe the EnKF in the ensemble-matrix notation, we split $\mathbf{D}$ and $\mathbf{G}$ into submatrices,

$$\mathbf{D} = \begin{pmatrix} \mathbf{D}^1 \\ \mathbf{D}^2 \\ \vdots \\ \mathbf{D}^{N_v} \end{pmatrix}, \quad \mathbf{G} = \begin{pmatrix} \mathbf{G}^1 \\ \mathbf{G}^2 \\ \vdots \\ \mathbf{G}^{N_v} \end{pmatrix}, \tag{24}$$

where N_v denotes the number of data groups, $\mathbf{D}^v$ denotes the ensemble matrix for data group number v and $\mathbf{G}^v$ denotes the ensemble matrix for the corresponding forward model. Furthermore, let $\mathbf{M}^v$ denote $\mathbf{M}$ after assimilation of v data groups have been completed, that is, $\mathbf{M}^v$ contains a sample from $p(\mathbf{m}^v|\mathbf{d}^{1:v})$. The EnKF equations for cycle number v may then be written as

$$\mathbf{W}^v = \mathbf{G}^v\left(\mathbf{M}^{v-1}\right), \tag{25}$$

$$\widetilde{\mathbf{K}}^v = \widetilde{\mathbf{C}}_{m^{v-1}w^v}\left(\widetilde{\mathbf{C}}_{w^v} + \mathbf{C}_{d^v}\right)^{-1}, \tag{26}$$

$$\mathbf{M}^v = \mathbf{M}^{v-1} + \widetilde{\mathbf{K}}^v\left(\mathbf{D}^v - \mathbf{W}^v\right). \tag{27}$$

After cycle number N_v, one obtains the final updated model ensemble $\mathbf{M}^{N_v}$, from which one may calculate empirical approximations to the two first moments of the posterior PDF, $p(\mathbf{m}^{N_v}|\mathbf{d}^{1:N_v})$, in a similar manner as described in the final paragraph of Section 3.2.2.

Note that the computational expense is approximately equal to N_e times the computational expense of one forward-model run for EnKF, and $(N_u \cdot N_e)$ times the computational expense of one forward-model run for ES-MDA. Hence, ensemble-based methods are suitable for problems with large N_m and N_d.

3.3 Sequential utilization of different data types

Seismic P-wave velocity depends on saturation and pressure. We will not invert for saturation or pressure changes directly, but rather invert for time-lapse changes in the geophysical parameter functions, σ, ρ, and V_p. In particular, we will use inversion results for σ and ρ to improve inversion results for V_p. If desired, saturation and pressure effects can be inferred from these inversion results.

Utilizing the notation from Section 3.1, we let q denote one of the geophysical parameter functions. We will consider changes in q from before injection starts (where the reservoir pressure is constant), and until after CO_2-injection has been active for some time. If rock properties were homogeneous, q^0 would then be constant, and spatial variations in $q-q^0$ would be identical to the spatial variations in q itself. For reasons given in Section 4.1, we will use homogeneous rock properties in the numerical experiments. Later on when we present results from the numerical experiments, we will therefore plot q and not $q-q^0$. Furthermore, we will not differentiate in the text between a geophysical parameter function and its time-lapse change, except if it is deemed necessary to avoid misunderstandings.

In the very early phase of a CO_2 injection, a pressure front is advancing, followed by a saturation front which is advancing much more slowly. Hence, in a later phase, no pressure front is found in the vicinity of the advancing saturation front. So, except in the very early stages, the pressure variation during CO_2 injection in a reservoir has a different character than the saturation variation, which defines the CO_2 plume.

These characteristics are reflected in the true V_p, depending on the rock physics. It may, however, be difficult to identify them in the V_p obtained by inverting seismic data, due to data and modeling errors and instability of the inversion. In particular, using a pixel parameterization to represent V_p may result in pixel-scale errors that blur the underlying large-scale CO_2 plume. The parameterization we apply here, however, directly represents large-scale structures, like a CO_2 plume. This means that while the inversion may not ensure a correct placement and shape of the plume, it will by construction of the parameterization avoid blurring of the plume by pixel-scale errors.

Electric conductivity depends on saturation, but not on pressure. Density depends on saturation and pressure. The variation in ρ across the CO_2-plume boundary is, how-

ever, significantly stronger than the variation due to pressure differences at neighbouring locations. Abrupt changes in σ or ρ with $\mathbf{x}$ therefore indicate the location of the CO_2-plume boundary (at least when using the parameterization described in Section 3.1, since pixel-scale errors then are avoided). The resolution with which σ and ρ can be determined from CSEM and gravimetric data, respectively, is, however, coarser than that with which V_p can be determined from seismic data. It is therefore not straightforward to utilize information about the CO_2 plume obtained from CSEM or gravimetric inversion in the seismic inversion. It would, for example, not be advisable to fix the CO_2-plume boundaries to those obtained from CSEM or gravimetric inversion when inverting the seismic data.

In Landrø & Zumberge (2017), a sequential approach for CO_2 estimation in the Sleipner field was proposed, where seismically derived saturation changes were used as input to gravity modeling. Part of the background for their approach was that time-lapse pore pressure changes were moderate at Sleipner, so that saturation effects dominate. A main aim for the Skade modeling study, motivating our work, is to investigate large-scale CO_2 injection with a small/realistic number of injection wells, such that large pressure effects must be anticipated. Our 'end product' is the seismic-velocity estimate, and we are just as interested in the pressure effect reflected in the seismic velocity as in the saturation effect. We therefore suggest an alternative sequential, two-step inversion strategy for joint utilization of CSEM or gravimetric data with seismic data. The main idea with the sequential procedure is to first gain knowledge about the location and shape of the CO_2 plume using CSEM or gravity data, which are both mainly influenced by saturation changes, and have lower resolution than seismic data. Subsequently, this knowledge is utilized to obtain an improved prior model for the seismic inversion, where we aim to obtain good estimates of both saturation-induced and pressure-induced changes in V_p. Implementation of this knowledge into the prior model for V_p is facilitated by using the same parameterization to represent σ, ρ, and V_p.

We summarize the two-step, sequential inversion strategy as follows:

Step 1: Invert CSEM or gravimetric data to get an approximate location and shape of the CO_2 plume

Step 2: Invert seismic data with prior information on the location and shape of the plume from step 1.

Note that we do not gain knowledge about variation of V_p with pressure from CSEM or gravity inversion. Hence, when making the prior model for seismic inversion, information on pressure effects on V_p must be apprehended from other sources, e.g., converting reservoir simulation results to seismic velocity via rock physics relations.

The sequential inversion strategy shares common themes with many current seismic full-waveform inversion schemes. There, low-frequency inversion results are used to get information on the general structures, which in turn are used to build initial models for subsequent high-frequency inversions. Hence, our two-step, sequential inversion strategy could be adapted in the case of seismic full-waveform inversion with step 1 using low-frequency seismic inversion, possibly together with CSEM or gravimetric inversion, and high-frequency seismic inversion in step 2.

4 Numerical experiments

The inversion methodology described in Section 3 was applied to synthetic data generated from simulated CO_2 injection in the Skade formation. The sequential inversion strategy described in Section 3.3 was employed in two separate test cases: one where step 1 was performed with CSEM inversion, and the other where step 1 was performed with gravity inversion. We compared the inversion results from the two acquisition methods in step 1. Subsequently, we wanted to assess how the different prior models from step 1 influenced on the final results of step 2. Finally, the performance of the sequential inversion strategy was compared with seismic inversion *without* any prior information from CSEM or gravity inversion results.

The EnKF was used to perform CSEM and seismic inversions, while the ES-MDA was used in the gravity inversion. The reason for choosing the ES-MDA for gravity inversion is that no reasonable way of grouping the data was found; see the brief discussion on data grouping in Section 4.2. The ES-MDA is computationally more expensive than the EnKF: the computational cost of one assimilation cycle in the ES-MDA equals the total computational cost of the EnKF. However, the gravity forward model has a low computational cost, which made the use of the ES-MDA feasible.

Following the reasoning laid out in Section 3.3, q for the CSEM and seismic inversions were σ and V_p, respectively. For gravity inversion, $\Delta\rho$ will play the role that q had

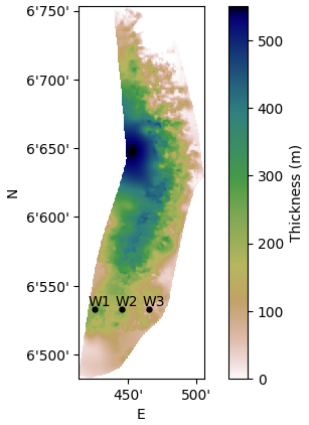

Figure 1. Thickness map of the Skade formation with the 3 injection wells — W1, W2, and W3 — marked

in Section 3.3, since processed gravimetric data is always a gravity anomaly, Δg_z (c.f. Section 2.2).

Since a total of three seismic inversions were conducted, a shorthand label for each one is given as follows: AVO_c is short for step 2 with prior information from CSEM inversion results; AVO_g is short for step 2 with prior information from gravity inversion results; and AVO_w denotes seismic inversion without prior information from either CSEM or gravity inversion results.

4.1 Skade formation and synthetic data generation

Together with the Ve Member, the Utsira Formation, and Upper Pliocene sands of the Nordland Group, the Skade Formation forms the outer part of a large deltaic system with its source area on the East Shetland Platform. The Skade Formation, Lower Miocene, consists of marine sandstones deposited over a large area of the Viking Graben. The maximum thickness is more than 500 m and the thickness decreases rapidly towards the east, where the sands terminate towards large Oligocene shale diapirs. Based on available pore volume, the estimated storage capacity of CO_2 in the Skade formation is approximately 15 Gton (Bøe et al., 2002).

To simulate large-scale CO_2 injection in the Skade formation, the commercial reservoir simulator Eclipse™ (Schlumberger Ltd., 2009), was used. The 3D reservoir model was set up following Elenius et al. (2018). The formation has not been well character-

ized geologically; thus, the porosity and permeability are assumed to be homogeneous with values taken within the range of Utsira sand data. Specifically, porosity was set to 0.16 while horizontal and vertical permeability were set to 1476 mD and 147.6 mD, respectively. Three injection wells were set up in the south part of Skade (see Figure 1), and CO_2 was injected over a 50-year period (year 2020–2070) with injection rate set as high as possible without exceeding the fracture pressure anywhere in the formation. (The fracture pressure was estimated based on rock-mechanical relations expected to be valid for the formation.) In total, approximately 3 Gton CO_2 was injected over the 50-year period.

The geophysical background model (i.e. *before* CO_2 injection) from the seabed to top Mjur formation was built using depth-converted seismic horizons and upscaled properties from a well log (15/9-3, located at the south end of the formation). In the CO_2 injection period, standard petrophysical relations described below were used to convert saturation and pressure to V_p, σ, and ρ. In the following, let subscripts 1 and 2 denote properties before and after CO_2 injection, respectively, and let the change in a generic property, τ, be denoted by $\Delta\tau = \tau_2 - \tau_1$. Furthermore, let S_{CO_2} denote saturation of CO_2 and P denote pressure. To generate the conductivity model, Archie's second law, assuming constant porosity, was used,

$$\sigma_2 = \sigma_1 \frac{(1 - S_{CO_2,1})^2}{(1 - S_{CO_2,2})^2}. \tag{28}$$

To generate P-wave velocity and density models, the following relationships from Landrø (2001) were used,

$$V_{p2} = V_{p1}(1 - k\Delta S_{CO_2} - l\Delta P - m\Delta P^2) \tag{29}$$

$$\rho_2 = \rho_1(1 - b\Delta S_{CO_2}). \tag{30}$$

In (29) and (30), b, k, l, and m are empirical parameters, which are given as

$$b = 0.05, \quad k = 0.1, \quad l = 0.0035, \quad m = -0.00003, \tag{31}$$

calculated from Utsira data. [Units of the parameters in (31) are clear from (29) and (30).] We note that the model in Landrø (2001) assumes that the coefficients in (31), which typically are calibrated against a few rock samples, are valid everywhere and independent of porosity. In Lang & Grana (2019), the author proposed an improved model, where they account for heterogeneous porosity, initial saturation, and pressure.

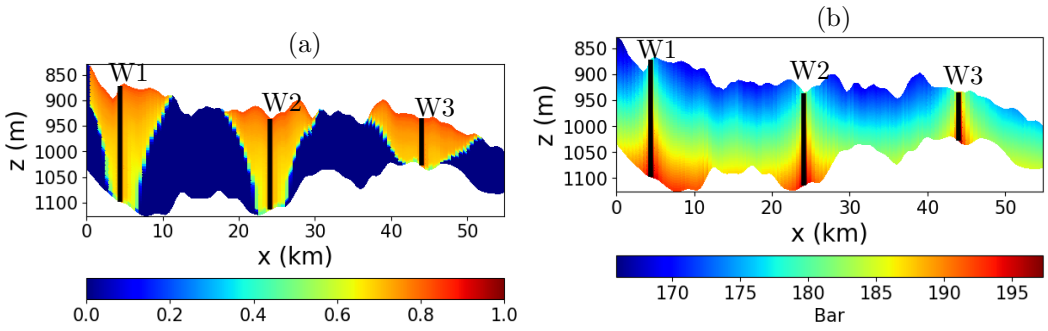

Figure 2. (a) S_{CO_2} and (b) P at year 2070. The vertical solid black lines indicate the wells, denoted W1, W2, and W3

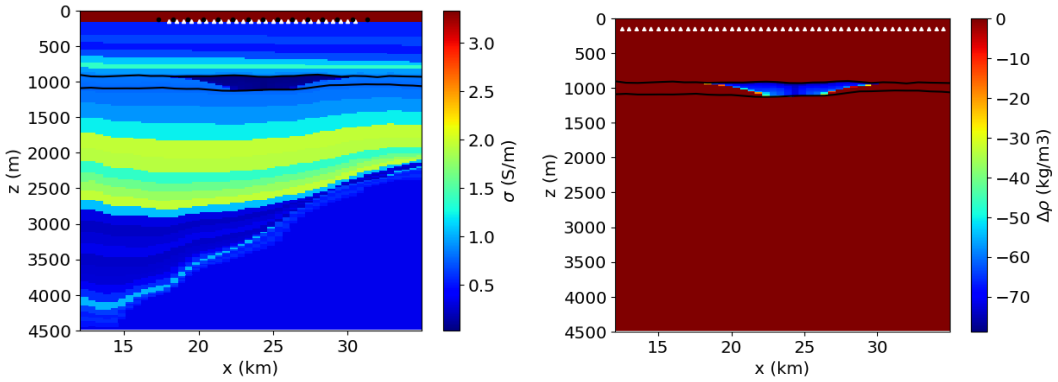

Figure 3. (a) σ and (b) $\Delta\rho$ in Γ at year 2070. Source positions (for CSEM) are indicated by $\bullet$ and receivers (for both CSEM and gravimetry) are indicated by $\triangle$. Note that Ω is outlined with a solid black line

To set up the monitoring test case, the true geophysical models were generated using S_{CO_2} and P from year 2070 (i.e., at the end of the CO_2 injection); confer Figure 2. We focused the test case area around injection well W2. To generate synthetic CSEM and gravity data, the commercial software COMSOL™ (COMSOL Inc., 2013), was used, while the reflection coefficient approximation described in Section 2.3 was used to generate the synthetic AVO data. Note that V_s in (10) was generated from V_p using a $\frac{V_p}{V_s}$ ratio of $\frac{\sqrt{14}}{2} \approx 1.8708$, which lies within the range for sandstone formations (Mavko et al., 2009).

4.2 Set up of experiments

In the numerical experiments, it was assumed that the geology was sufficiently well known such that Ω only includes the Skade formation, while geophysical parameters in $\Gamma \backslash \Omega$ (i.e. the computational domain outside the inversion domain) are fixed to the background model. For the CSEM inversion, σ in $\Gamma \backslash \Omega$ was given as seen in Figure 3a. For gravity inversion, $\Delta\rho$ in $\Gamma \backslash \Omega$ was zero; see Figure 3b. Gaussian random noise will be added to the data. For CSEM and gravity data, the noise standard deviation will be set relative to the magnitude of the data, see, e.g., Ray & Key (2012); Li & Oldenburg (1998). For seismic (reflection coefficient) data, however, we set the noise standard deviation to a fixed value. Alternative noise models are viable for all data types, and one may anticipate that the choice of noise models can influence on the estimation results. Since fixing the inversion region is a simplification of the inversion problem, we have tried to compensate by applying data error models that can be seen as conservative, see, e.g., Agersborg et al. (2017). A thorough investigation of the influence of data error models on inversion results is, however, beyond the scope of this chapter.

For the seismic inversions, the data are R_{pp} given on an equidistant grid within Ω with cell sizes $\Delta x = 500$ m and $\Delta z = 15$ m, hence no background model is needed. Note that in the following, CSEM and gravity data are contaminated with random noise relative to the magnitude of the data, similar to what is common in geophysical literature, see, e.g., Ray & Key (2012); Li & Oldenburg (1998). For seismic data, however, it is well known that amplitudes can be difficult to measure because of noise and problems with amplitude- and frequency-preserving processing. This, together with the fact that R_{pp} can often be zero, or very close to zero, leads us to choose a random noise with fixed variance for the seismic data.

The data used for the CSEM inversion, $\mathbf{e}_x$, were extracted at 26 sea-floor receivers, evenly distributed with 500 m intervals for $x \in (18000, 30500)$ m and $z = 150$ m. The source frequency was 0.25 Hz, and eight source positions, evenly distributed with 2000 m interval for $x \in (17300, 31300)$ m and $z = 120$ m, were applied; see Figure 3a. Five percent Gaussian noise with noise floor 10^{-15} V/Am^2 was added to the data. Furthermore, data from receivers less than 2000 m away from the source position were removed to avoid influence from the direct wave.

The data used for the gravity inversion, Δg_z, were extracted at 45 sea-floor receivers, evenly distributed with 500 m interval for $x \in (12500, 34500)$ m and $z = 150$ m; see Figure 3b. Ten percent Gaussian noise was added to the data.

The data used for the seismic inversions, R_{pp}, were extracted at $\theta = (5, 10, 15, 20, 25, 30)^\circ$. Recall from Section 2.3 that we have assumed that the θ's have been converted from source-receiver offsets in a processing step. Gaussian noise with standard deviation 0.007 was added to the data, which typically lie within the range $R_{pp} \in (0, 0.04)$.

For the CSEM inversion, the data were divided into a subset of eight groups ($N_v = 8$), where each group consisted of data obtained with one particular source position, resulting in 32 or 36 data points per group, depending on source-receiver distance. The first group corresponded to source position $(x, z) = (17300, 120)$ m, and the subsequent data groups followed the adjacent source positions as defined above. For the seismic inversions, the data were divided into six groups ($N_v = 6$), where each group consisted of data from one element in θ, resulting in 458 data points per group. The first group corresponded to $\theta_1 = 5^\circ$, and subsequent data groups followed the increasing angles up to 30°, as described above. Note that the ordering of data may influence the inversion results (Fossum & Mannseth, 2015), but obtaining the 'best' practice for grouping the data is beyond the scope of this chapter.

In the gravity inversion with the ES-MDA, all data are used simultaneously; 45 data points in total. (Gravity data can only be grouped by receiver position, thus only part of Ω would have been covered by each sequential step, had the EnKF been used.) The number of assimilation cycles were chosen as $N_u = 8$ and the inflation factor was chosen as $\eta_u = 1/N_u$ for $u \in [1, N_u]$. Optimal tuning of N_u and $\eta_{1:N_u}$ is beyond the scope of this chapter.

The representation given in Section 3.1 was applied to model two regions, leading to

$$q(\mathbf{x}; \mathbf{m}) = c_1 \chi_1(\mathbf{x}; \mathbf{a}) + c_2 \chi_2(\mathbf{x}; \mathbf{a}), \tag{32}$$

where $\mathbf{a}$ is specified such that χ_1 becomes the indicator function for the CO_2-plume region, and χ_2 becomes the indicator function for the region outside the plume. Hence, with this representation, q takes the value c_1 inside the plume and c_2 outside the plume.

For more details on how (32) works, we refer to Appendix A. Furthermore, the description of the experimental setup in the next three paragraphs assumes familiarity with some of the details in Appendix A. We think it should be possible to skip these paragraphs if the reader thinks that it is not necessary to grasp all details of the experimental setup before assessing the experimental results.

The shape of the modelled CO_2-plume boundary is given by $\zeta(\mathbf{x}, \mathbf{a})$ (defined in Appendix A), and $N_a = 45$ parameter grid nodes, evenly distributed over the Skade formation (nine parameter grid nodes in the x-direction from $x = 12000$ m to $x = 35000$ m, and five parameter grid nodes in z-direction from $z = 890$ m to $z = 1130$ m), were applied in (A4) to represent $\phi(\mathbf{x}, \mathbf{a})$.

Since it it assumed (see, Section 4.1) that σ is independent of pressure, and since the simulated CO_2 saturation does not vary much inside the plume, (A2) was used to represent σ in the CSEM inversion. Since the variation of $\Delta\rho$ with pressure is weak, (A2) was also used to represent $\Delta\rho$ in the gravity inversion.

Since the variation of V_p with pressure is more pronounced, V_p was represented with (A3) in the seismic inversion. We let $k_1(\mathbf{x}; \mathbf{c}_1)$ and $k_2(\mathbf{x}; \mathbf{c}_2)$ be given by (A4) with $N_{c_1} = N_{c_2} = 15$, and let the parameter grid nodes for $k_1(\mathbf{x}; \mathbf{c}_1)$ and $k_2(\mathbf{x}; \mathbf{c}_2)$ be evenly distributed over the same area as for the representation of $\phi(\mathbf{x}, \mathbf{a})$, but now with five nodes in x-direction and three in z-direction.

Initial ensembles for the CSEM, gravity, and AVO_w inversions were generated according to the description in Appendix B, with $N_e = 100$ for the CSEM and gravity inversions, and $N_e = 1000$ for the AVO_w inversion. (Initial ensembles for AVO_c and AVO_g are described in Sections 4.3.4 and 4.3.5, respectively.) The values for N_e used in the experiments were chosen such that $N_e > N_d$, to avoid problems with strong unwarranted reduction of the variability among ensemble members. (See, for example Chap. 14 in Evensen (2009) for a discussion of this issue, also known as ensemble collapse).

The mean prior model, $\bar{\mathbf{m}}^0$, was selected to reflect the situation just after the CO_2 injection started. The types of plots used to illustrate the prior means will occur repeatedly, and we now provide a brief explanation. Figure 4a shows the resulting plume boundaries (i.e. the zero level set, ζ, in the languague of Appendix A) at equal distances from the vertical injection well (not shown). The corresponding prior means (initial values)

Table 1. Input parameters for generation of $\mathbf{C}_{a^0}$. Note that the same $\mathbf{C}_{a^0}$ was used in the CSEM, gravity, and AVO_w inversions. Confer Appendix B for description of input parameters

α	β	γ	δ
8	20	45°	0.25

Table 2. Input parameters for generation of $\mathbf{C}_{c^0}$. Note that the unit for β is S/m for CSEM, kg/m^3 for gravity, and m/s for seismic inversion. Confer Appendix B for description of input parameters

Inversion	α	β	γ	δ
CSEM	-	0.01	-	-
Gravity	-	10	-	-
AVO_w	3	200	0°	0.25

for σ, $\Delta\rho$, and V_p are illustrated in Figure 4b – 4d. Note that the transitions in $\bar{\sigma}^0$ and $\bar{\Delta\rho}^0$ from $\bar{c}_1^0$ (blue color) to $\bar{c}_2^0$ (red color) when crossing one of the plume boundaries on Figure 4b and Figure 4c, respectively, are not sharp. This is because we, for reasons given in Appendix A, have introduced a smoothness across plume boundaries in the numerical realization of (32). From Figure 4d it is seen that $\bar{V}_p^0$ differs significantly from being constant within each region. This reflects that an extended version of (32), where the coefficients multiplying the basis functions are allowed to vary with $\mathbf{x}$, has been applied since V_p vary spatially also with pressure.

To generate $\mathbf{C}_{m^0}$ for the CSEM, gravity, and AVO_w inversions, it was assumed that the $\mathbf{C}_{c_1^0} = \mathbf{C}_{c_2^0} = \mathbf{C}_{c^0}$ and the input parameters in Table 1 and 2 were used. Recall that for CSEM and gravity inversions, $\mathbf{C}_{c^0}$ reduces to a variance, β, since (A2) was used.

4.3 Inversion results

In this section, inversion results using the sequential, two-step inversion methodology and AVO_w are presented. To make it easier to compare inversion results where different forward model simulators (with different discretizations) have been used, all inversion results are mapped onto a separate plotting grid. The plotting grid was made

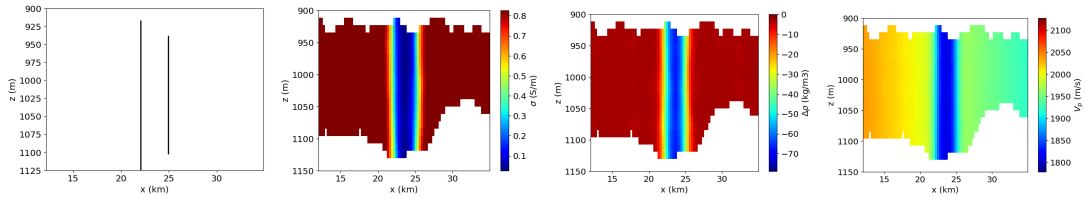

(a) (b) (c) (d)

Figure 4. (a) ζ generated using $\bar{\mathbf{a}}^0$. (b) σ, (c) $\Delta\rho$, and (d) V_p models made with $\bar{\mathbf{m}}^0$ for the CSEM, gravity, as AVO_w inversions, respectively

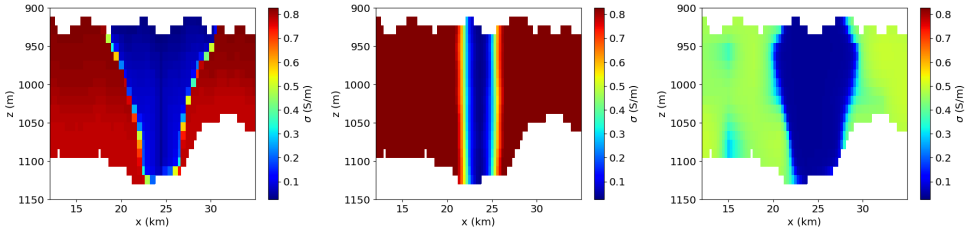

(a) (b) (c)

Figure 5. Step 1 CSEM inversion. (a) true σ. Mean of the (b) initial and (c) final updated σ

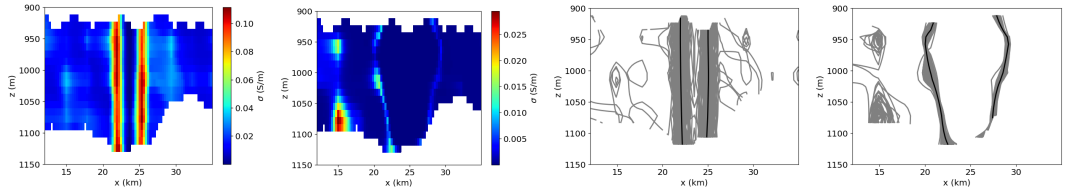

(a) (b) (c) (d)

Figure 6. Step 1 CSEM inversion. Variance of the (a) initial and (b) final updated σ; ζ generated using ensemble mean (solid black) and members (grey) from the (c) initial and (d) final ensemble

using equidistant grid cells in x- and z-direction, covering Ω. Furthermore, the figures have been vertically exaggerated.

4.3.1 Step 1: CSEM inversion

The true σ for the CSEM inversion is shown in Figure 5a. Figure 5b and 5c show means of the initial and final updated σ. From Figure 5c it is seen that shape of the CO_2 plume, given by the low-conductivity structure, has good correspondence with the true

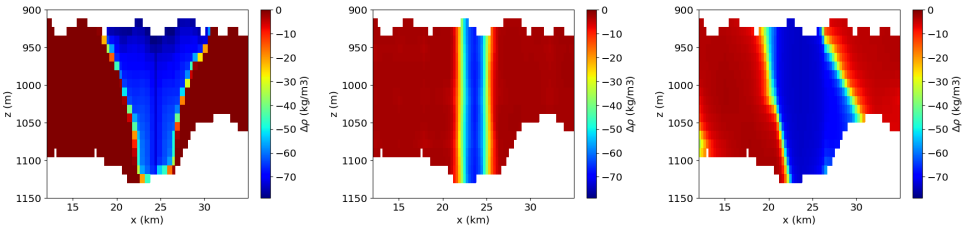

(a) (b) (c)

Figure 7. Step 1 gravity inversion. (a) True $\Delta\rho$. Mean of the (b) initial and (c) final updated $\Delta\rho$

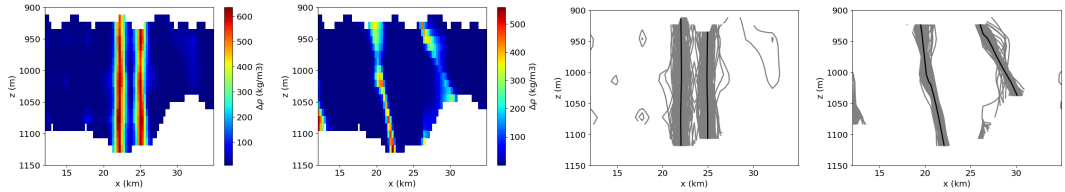

(a) (b) (c) (d)

Figure 8. Step 1 gravity inversion. Variance of the (a) initial and (b) final updated $\Delta\rho$; ζ generated using ensemble mean (solid black) and members (grey) from the (c) initial and (d) final ensemble

shape of the plume, with some deviations at the top of the formation. The conductivity of the CO_2 is well estimated, while the brine conductivity is underestimated.

In Figure 6a and 6b, it is seen that the variance of σ has been reduced significantly. Some high variance, relative to other areas, can be seen on the left side of the formation, indicating higher model uncertainty in this area. In the following sections, similar type of plots like Figure 6c and Figure 6d will occur, and we thus provide a brief explanation. The black curves on Figure 6c and Figure 6d show the corresponding means of the initial and final updated CO_2-plume boundaries, respectively, while each grey curve shows the plume boundary for a single ensemble member. The spread of the initial ensemble members, shown in Figure 6c, has been much reduced in the final ensemble, see Figure 6d, again indicating a reduction in model uncertainty.

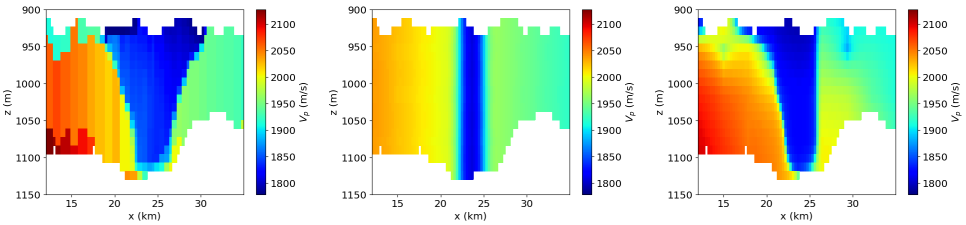

(a) (b) (c)

Figure 9. AVO_w inversion. (a) True V_p. Mean of the (b) initial and (c) final updated V_p

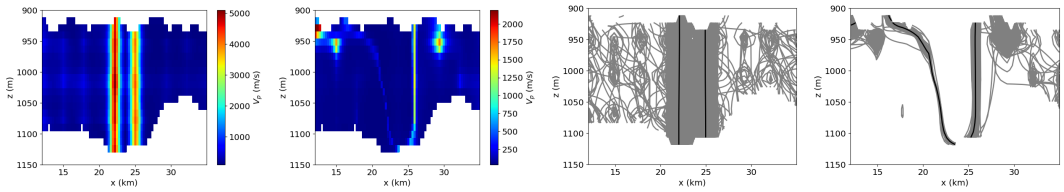

(a) (b) (c) (d)

Figure 10. AVO_w inversion. Variance of the (a) initial and (b) final updated V_p; ζ generated using ensemble mean (solid black) and members (grey) from the (c) initial and (d) final ensemble

4.3.2 Step 1: Gravity inversion

In Figure 7b and 7c, the mean of the initial and final updated $\Delta\rho$ is shown. Comparing Figure 7c with the true $\Delta\rho$ in Figure 7a, it is seen that the shape of the CO_2 plume is not well approximated on the right side, while on the left side it is closer to the true shape. It is also seen that the $\Delta\rho$ values outside the CO_2 plume are well approximated in most areas, except a small area in the bottom left corner of the formation.

From Figure 8a and 8b, it is seen that there are areas where the variance has not been reduced much from initial to final ensemble, especially around the CO_2 plume front. Figure 8c and 8d, show that the spread of the ensemble members from initial to final has been reduced to some extent. In total, Figure 8a – 8d show that the model uncertainty has only been partially reduced in the ensemble-based inversion, and that the areas where the estimation deviates most from the true $\Delta\rho$ have the highest uncertainty.

4.3.3 AVO_w

Before assessing the inversion results from step 2 with AVO_c and AVO_g, the results from AVO_w is presented. The means of the initial and final updated V_p are shown in Fig-

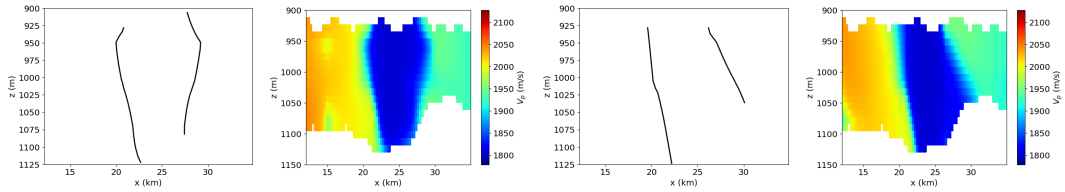

(a) (b) (c) (d)

Figure 11. ζ generated using $\bar{\mathbf{a}}^0$ for (a) AVO_c and (c) AVO_g; and V_p for (b) AVO_c and (d) AVO_g made with $\bar{\mathbf{m}}^0$

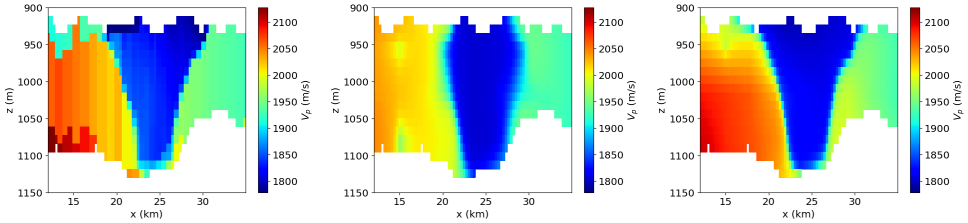

(a) (b) (c)

Figure 12. AVO_c inversion. (a) True V_p. Mean of the (b) initial and (c) final updated V_p

ure 9b and 9c. Comparing the mean of the final updated V_p with the true V_p in Figure 9a, it is seen that the left side of the formation is well approximated, while the CO_2 plume (given by the low-velocity shape) is not well approximated on the right side of the formation.

From Figure 10a and 10b, it is seen that the variance has been reduced much except in a few areas at the top of the formation. Looking at Figure 10c and 10d, it is seen that the spread of the ensemble members has been reduced much, especially for the left CO_2 front, while significant model uncertainty can be seen on the right side and top left of the formation. The areas with highest uncertainty are where the deviation of the final updated V_p is largest compared with the true V_p.

4.3.4 Step 2: AVO$_c$

Following the sequential, two-step inversion strategy, knowledge about the location of the CO_2 plume from the CSEM inversion was used to make the prior model for AVO_c. Specifically, the mean of the final updated $\mathbf{a}$ from the CSEM inversion was used as $\bar{\mathbf{a}}^0$ in AVO_c. Figure 11a shows ζ generated with $\bar{\mathbf{a}}^0$. Since V_p depends on both saturation

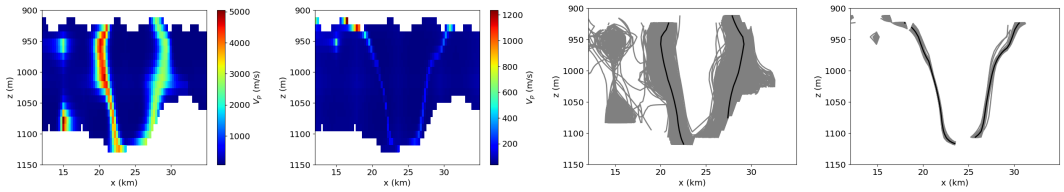

(a) (b) (c) (d)

Figure 13. AVO_c inversion. Variance of the (a) initial and (b) final updated V_p; ζ generated using ensemble mean (solid black) and members (grey) from the (c) initial and (d) final ensemble

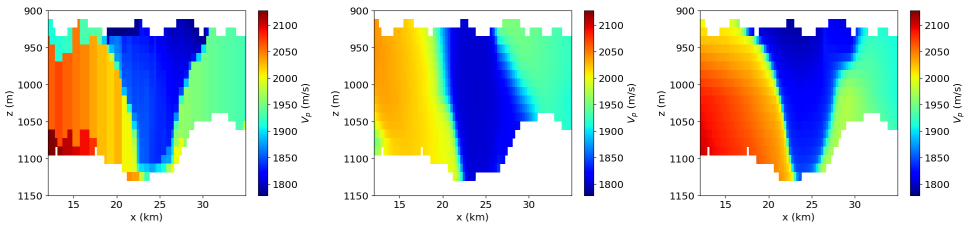

(a) (b) (c)

Figure 14. AVO_g inversion. (a) True V_p. Mean of the (b) initial and (c) final updated V_p

and pressure, and we do not gain information on pressure from CSEM inversion, we let $\bar{\mathbf{c}}^0$ be the same as for AVO_w, see Figure 11b. (If we have had information on pressure from, e.g., well measurements, a better $\bar{\mathbf{c}}^0$ could be made.) The initial ensemble was generated with 1000 realizations, where $\mathbf{C}_{a^0}$ and $\mathbf{C}_{c^0}$ were the same as given for AVO_w in Table 1 and 2, except $\beta = 10$ for $\mathbf{C}_{a^0}$ (to reflect that the step 1 inversion has reduced the prior uncertainty in step 2 for the shape of the CO_2 plume).

In Figure 12b and 12c, the means of the initial and final ensembles are shown. Comparing Figure 12c with the true V_p in Figure 12a, it is seen that mean of the final updated V_p approximates the true V_p well, both in terms of the shape of the CO_2 plume and V_p distribution inside and outside the CO_2 plume.

From Figure 13a and 13b, it is seen that the variance has been reduced much from initial to final ensemble. A similar conclusion can be made by looking at the spread of the initial and final ensemble members in Figure 13c and 13d, where it is seen that the uncertainty in the shape of the CO_2 plume is small.

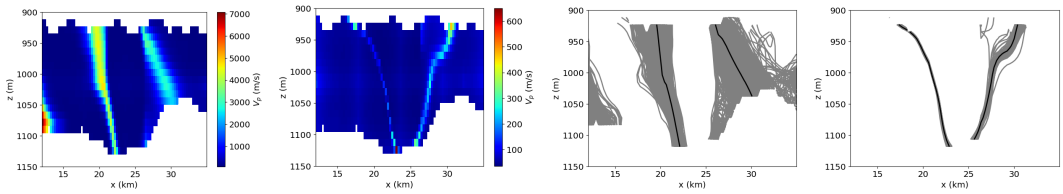

Figure 15. AVO_g inversion. Variance of the (a) initial and (b) final updated V_p; ζ generated using ensemble mean (solid black) and members (grey) from the (c) initial and (d) final ensemble

4.3.5 Step 2: AVO_g

To generate the initial ensemble for AVO_g, the same procedure as for AVO_c, discussed in Section 4.3.4, was used: $\bar{\mathbf{a}}^0$ was given as the mean of $\mathbf{a}$ from the final ensemble in step 1, while $\bar{\mathbf{c}}^0$ was the same as for AVO_w (following the same arguments as in AVO_c); see Figure 11c and 11d. Furthermore, $\mathbf{C}_{c^0}$ and $\mathbf{C}_{a^0}$ were the same as in AVO_c, and 1000 realizations were generated for the initial ensemble.

The means of the initial and final ensembles are shown in Figure 14b and 14c, and it is seen in Figure 14c that the shape of the CO_2 plume and the V_p distribution approximate the true V_p in Figure 14a well.

Looking at Figure 15a and 15b, it is seen that the variance has been reduced much from initial to final ensemble, with some higher variance around the right CO_2 plume front. From Figure 15c and 15d it is seen that the spread of the ensemble members has been reduced much, especially around the left front of the CO_2 plume.

4.3.6 Data misfit

To make a quantitative comparison of AVO_w, AVO_c, and AVO_g, we calculate the data misfit using ensembles from all three inversions. The data misfit for a single ensemble member, $\mathbf{m}_j$, is calculated as,

$$O_j = (\mathbf{d} - \mathbf{g}(\mathbf{m}_j))^T \mathbf{C}_d^{-1} (\mathbf{d} - \mathbf{g}(\mathbf{m}_j)), \tag{33}$$

where $\mathbf{d}$ denote the seismic AVO data for all θ, $\mathbf{g}(\mathbf{m}_j)$ denote the corresponding forward model predictions, $\mathbf{C}_d$ denotes a $N_d \times N_d$ diagonal matrix with diagonal entries equal to $5{\cdot}10^{-5}$, and $j = 1, 2, \ldots, N_e$. Let $\mathbf{m}^{init}$ and $\mathbf{m}^{final}$ denote initial and final updated

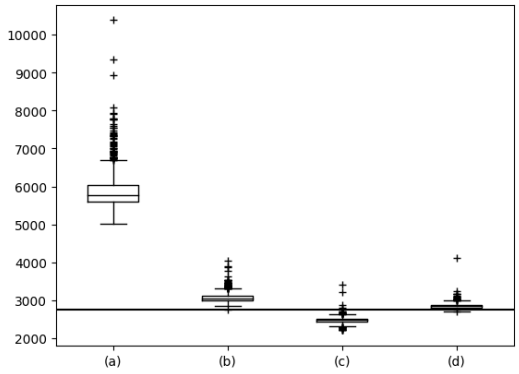

Figure 16. Data misfit using initial ensemble from (a) $\mathrm{AVO_w}$; and final updated ensembles from (b) $\mathrm{AVO_w}$, (c) $\mathrm{AVO_c}$, and (d) $\mathrm{AVO_g}$. The box extend from the 25th (Q1) to the 75th (Q3) percentile with the central line denoting median. The whiskers extend from Q1 to 1.5·Q1 and from Q3 to 1.5·Q3, and points (+) beyond the whiskers are considered outliers. The horizontal line denotes $N_d = 2748$

parameter ensembles, respectively, and let O_j^{init} and O_j^{final} denote the corresponding values of O_j. In Figure 16, $\{O_j^{final}\}_{j=1}^{N_e}$ for $\mathrm{AVO_w}$, $\mathrm{AVO_c}$, and $\mathrm{AVO_g}$ are compared to each other and with $\{O_j^{init}\}_{j=1}^{N_e}$ for $\mathrm{AVO_w}$. ($\{O_j^{init}\}_{j=1}^{N_e}$ for $\mathrm{AVO_c}$ and $\mathrm{AVO_g}$ were similar to that for $\mathrm{AVO_w}$, and are therefore not shown.) We see that the data misfit from all three inversions has been reduced much from initial to final updated ensembles, and end up close to N_d (often used as solution criteria in inversion algorithms within the classical inversion framework). Comparing $\{O_j^{final}\}_{j=1}^{N_e}$ from $\mathrm{AVO_w}$ to $\mathrm{AVO_c}$ and $\mathrm{AVO_g}$, we see that they are statistically similar.

4.4 Discussion

In the seismic inversions done in this chapter, the data variance was set to an absolute value of $5 \cdot 10^{-5}$. We have performed seismic inversions with different absolute values for the data variance and similar results as shown in Section 4.3 were obtained.

The numerical results shown in this section are based on a large-scale CO_2 injection study where the goal was to inject as much CO_2 as possible without creating hazardous over-pressure that can lead to, e.g., fault reactivation, and fracturing. We have also applied the sequential inversion strategy in a preliminary CO_2 injection study, where a relatively small amount of CO_2 was injected (not shown here). Here, the benefit of the

sequential, two-step inversion strategy over just performing seismic inversion was not so clear. Since the spatial resolution of CSEM and gravimetry is lower than that of seismic, and the sensitivities of these methods are dependent on the amount of CO_2 injected, there will be a point where the benefit of performing CSEM or gravity inversion prior to seismic inversion will be minimal.

5 Conclusions

In this chapter, we have extended the work presented in Tveit et al. (2020) with introductory text on the CSEM experiment and forward modeling, parameterization of the unknown parameter functions, and ensemble-based methods for inversion. The introductory text served as foundation for our Bayesian sequential inversion strategy for joint utilization of CSEM or gravimetric data with seismic AVO data. The inversion methodolgy was applied to a test case based on simulation of large-scale CO_2 injection in the Skade formation. The strategy consists of two steps: In step 1, we invert CSEM or gravity data to get an approximate location and shape of the CO_2 plume, and in step 2, the inversion result from step 1 is used in the construction of the prior model for seismic AVO inversion.

The unknown geophysical parameter functions — electric conductivity, density, and seismic velocity — are represented using a carefully designed parameterization. The parameterization is based on the level-set framework which allows for representation of region boundaries defined by the large-scale CO_2 plume and slowly varying geophysical properties inside and outside the plume. By using parameter grids detached from the forward-model grid, the parameterization uses far less parameters in the inversion compared with equivalent methodologies using a pixel-based parameterization.

To solve the inverse problems considered in this chapter, ensemble-based Bayesian methods are used. For CSEM and seismic inversions we applied the EnKF, while ES-MDA was used for gravity inversion. Both these ensemble-based methods provide an approximate sample from the true posterior PDF at moderate computational cost.

Numerical results from step 1 of the inversion strategy showed that inversion of CSEM data provided a better approximation of the shape and location of the CO_2 plume than inversion of gravimetric data. Numerical results from step 2 of the inversion strategy showed, however, that the seismic velocity model was well identified using prior information from

either CSEM or gravity inversion results. Numerical results from seismic AVO inversion *without* any prior information from CSEM or gravity inversion showed that the seismic velocity model was only partially recovered. Hence, utilizing CSEM or gravity data with seismic AVO data with the sequential inversion strategy improved the seismic inversion results significantly.

Appendix A Reduced, smoothed level-set representation

Recalling the notation introduced in Section 3.1, let $\{\phi_i\}_{i=1}^{N_\phi}$ denote a set of real-valued, continuous functions on Ω — the *level-set (LS) functions*. Utilizing this set to construct $\{\Omega_j\}_{j=1}^{N_c}$ in a particular manner will render (12) a *LS representation*. With $N_c > 2$, alternative LS representations (LSR)s exist (Vese & Chan, 2002; Litman, 2005; Dorn & Villegas, 2008; Mannseth, 2014) which are able to represent between $N_\phi+1$ and 2^{N_ϕ} subregions using N_ϕ LS functions. For detailed expositions of the LSRs proposed by Vese & Chan (2002) and Mannseth (2014) in the context of modeling of geophysical exploration problems, we refer to Tveit et al. (2015b) and Tveit et al. (2015a), respectively. We will, however, only require the case where $N_c = 2$, in which case the LSR is unique and only a single LS function, ϕ, is applied.

To arrive at the LS representation from (12) with $N_c = 2$ inserted, we first replace the explicit dependence of χ_1 and χ_2 on $\mathbf{x}$ and $\mathbf{a}$ by an implicit dependence through the LS function,

$$q(\mathbf{x};\mathbf{m}) = c_1\chi_1(\phi(\mathbf{x};\mathbf{a})) + c_2\chi_2(\phi(\mathbf{x};\mathbf{a})). \tag{A1}$$

Next, we select Ω_1 as the part of Ω where $\phi(\mathbf{x};\mathbf{a}) > 0$. Since $\Omega_2 = \Omega \setminus \Omega_1$, we obtain the LSR in standard notation,

$$q(\mathbf{x};\mathbf{m}) = c_1 H(\phi(\mathbf{x};\mathbf{a})) + c_2(1 - H(\phi(\mathbf{x};\mathbf{a}))), \tag{A2}$$

where H denotes the Heaviside function (indicator function for the positive real axis). There are few restrictions on ϕ. Hence, the LSR is a very flexible way to represent subregions in Ω, as illustrated in Figure A1.

The shapes of Ω_1 and Ω_2 are governed by the LS function, whose spatial variation is controlled by the parameters in $\mathbf{a}$.

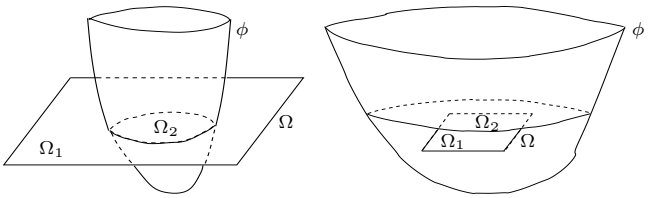

Figure A1. Two arbitrary instances of the LSR with $N_c = 2$

The LSR has been extended (Dorn & Villegas, 2008) to incorporate arbitrary spatial variation within each zone by replacing (A2) with

$$\begin{aligned} q(\mathbf{x};\mathbf{m}) &= k_1(\mathbf{x};\mathbf{c}_1)\, H(\phi(\mathbf{x};\mathbf{a})) \\ &+ k_2(\mathbf{x};\mathbf{c}_2)\,(1 - H(\phi(\mathbf{x};\mathbf{a}))), \end{aligned} \tag{A3}$$

where $\mathbf{c}_1 \in \mathbb{R}^{N_{c_1}}$, $\mathbf{c}_2 \in \mathbb{R}^{N_{c_2}}$, and $N_{c_1} + N_{c_2} = N_c$. Both (A2) and (A3) will be applied in numerical examples, where relevant quantities, such as N_{c_1} and N_{c_2}, will be specified. To complete the general description of the LSR, the dependency of ϕ on $\mathbf{x}$ and $\mathbf{a}$ must be specified. When applying (A3), also the dependencies of k_1 on $\mathbf{x}$ and $\mathbf{c}_1$ and k_2 on $\mathbf{x}$ and $\mathbf{c}_2$ must be specified. We will apply the same type of representation for the LS function, ϕ, as for the coefficient functions, k_1 and k_2.

A1 Reduced parameterization of level-set and coefficient functions

Let ψ represent either of the functions ϕ, k_1, or k_2, and correspondingly, let $\mathbf{b}$ represent either $\mathbf{a}$, $\mathbf{c}_1$, or $\mathbf{c}_2$. We express the dependency of ψ on $\mathbf{x}$ and $\mathbf{b}$ by (Berre et al., 2009)

$$\psi(\mathbf{x};\mathbf{b}) = \sum_{k=1}^{N_b} b_k \xi_k(\mathbf{x}). \tag{A4}$$

The basis functions $\{\xi_k\}_{k=1}^{N_b}$ are defined on a rectangular parameter grid that is not attached to, and much coarser than, the forward-model grid (Figure A2a). Hence, $N_b \ll N_g$, and our parameterization is therefore significantly reduced with respect to a pixel parameterization. There will, however, still be sufficient flexibility to approximately represent the large-scale structures that we aim to estimate.

While alternative representations are viable, we represent ψ in a finite-element fashion (Berre et al., 2009), and let ξ_u be a normalized piecewise bilinear function with sup-

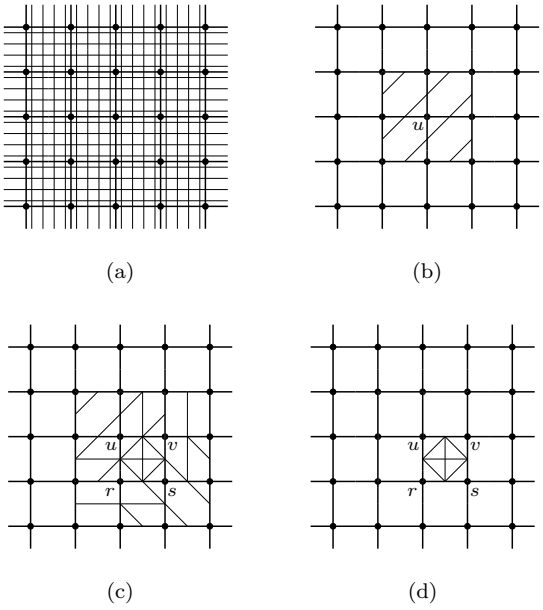

Figure A2. (a) Schematic detail of parameter grid (thick lines) and forward-model grid (thin lines). (b) Support of ξ_u (/). (c) Supports of ξ_u (/); ξ_v (|); ξ_r (−) and ξ_s (\). (d) Element where ξ_u, ξ_v, ξ_r and ξ_s have common support

port on the four rectangular elements adjacent to node u (arbitrary) (Figure A2b). Its value is unity in node u and zero in all other nodes. Figure A2c shows node u and three of its adjacent nodes, v, r, and s, and the supports of the basis functions associated with these four nodes. Figure A2d shows the element where ξ_u, ξ_v, ξ_r, and ξ_s have common support. The projections of ξ_u, ξ_v, ξ_r, and ξ_s onto this element are normalized bilinear functions, so whenever ψ is to be evaluated at a forward-model grid point, its value is calculated using bilinear interpolation.

A2 Smoothed level-set representation

We replace H in the LSR by a smoothed approximation,

$$\widetilde{H}(\phi) = \frac{1}{\pi}\tan^{-1}(\phi) + \frac{1}{2}, \tag{A5}$$

resulting in $q(\mathbf{x};\mathbf{m})$ no longer being a zonation since $\widetilde{H}$ will have global support in Ω. Introducing smoothness in q can be benificial since the nonlinearity in the mapping $\mathbf{a} \rightarrow q$ will decease with increasing smoothness (Lien et al., 2005). This consideration should, however, be balanced by the desire to keep a relatively sharp transition between subre-

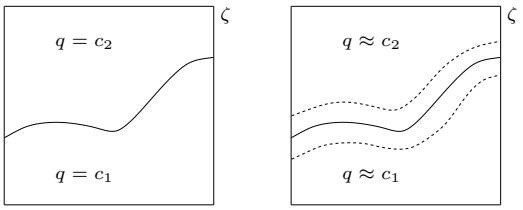

(a) (b)

Figure A3. Sketch of arbitrary $q(\mathbf{x};\mathbf{m})$ in the vicinity of ζ. (a) LSR and (b) smoothed approximation to a LSR, with transition region indicated by dashed curves.

gions where $q(\mathbf{x};\mathbf{m}) \approx c_1$ ($q(\mathbf{x};\mathbf{m}) \approx k_1(\mathbf{x};\mathbf{c})$ if (A3) is applied) and subregions where $q(\mathbf{x};\mathbf{m}) \approx c_2$ ($q(\mathbf{x};\mathbf{m}) \approx k_2(\mathbf{x};\mathbf{c})$ if (A3) is applied). The width of the transition region is decided by the behaviour of ϕ in the vicinity of its zero-level set, ζ. Let $\mathbf{n}$ be a unit normal vector to ζ. A sharp transition in q over ζ then corresponds to large values of $|\nabla\phi\cdot\mathbf{n}|$. Figure A3 illustrates the difference between a LSR and a smoothed approximation to a LSR when (A2) is applied.

Appendix B Initial ensemble generation

The ensemble-based inversion methodologies described in Section 3.2 require generation of an initial ensemble. The initial ensemble is generated from the prior PDF, $p(\mathbf{m}^0)$, which is chosen to be Gaussian,

$$p(\mathbf{m}^0) \sim \mathcal{N}(\bar{\mathbf{m}}^0, \mathbf{C}_{m^0}). \tag{B1}$$

Standard Cholesky decomposition method can thus be used to generate realizations from $p(\mathbf{m}^0)$,

$$\mathbf{m}_j = \bar{\mathbf{m}}^0 + \mathbf{L}\mathbf{z}_j, \quad j = 1, \ldots, N_e, \tag{B2}$$

where $\mathbf{z} \sim \mathcal{N}(0,1)$ and $\mathbf{L}\mathbf{L}^T = \mathbf{C}_{m^0}$, with $\mathbf{L}$ being a lower triangular matrix. Based on knowledge of the CO_2plume, e.g. from previous time-lapse vintage data, suitable values for $\bar{\mathbf{m}}^0 = ((\bar{\mathbf{c}}^0)^T, (\bar{\mathbf{a}}^0)^T)^T$ can be generated. To generate $\mathbf{C}_{m^0}$, it is assumed that $\mathbf{a}$ and $\mathbf{c}$ are not correlated, and, moreover, it is assumed that $\mathbf{c}_1$ is not correlated with $\mathbf{c}_2$. Hence,

$$\mathbf{C}_{m^0} = \begin{bmatrix} \mathbf{C}_{c_1^0} & \mathbf{0} & \mathbf{0} \\ \mathbf{0} & \mathbf{C}_{c_2^0} & \mathbf{0} \\ \mathbf{0} & \mathbf{0} & \mathbf{C}_{a^0} \end{bmatrix}, \tag{B3}$$

where $\mathbf{C}_{c_i^0}$ and $\mathbf{C}_{a^0}$ denote covariance matrices for $\mathbf{c}_i$, $i = 1, 2$, and $\mathbf{a}$, respectively. Note that if (A2) is applied, the covariance matrix $\mathbf{C}_{c_i^0}$ reduces to a scalar variance, β_i.

To generate $\mathbf{C}_{c_i^0}$ and $\mathbf{C}_{a^0}$, a spherical covariance function (Chilès & Delfiner, 2012),

$$C(h) = \beta \begin{cases} 1 - \frac{3h}{2\alpha} + \frac{h^3}{2\alpha^3}, & \text{for } 0 \leq h \leq \alpha, \\ 0, & \text{for } h > \alpha, \end{cases} \tag{B4}$$

is applied. Here, h denotes spatial distance between two nodes in the parameter grid (confer Section A1), and α denotes the correlation length. The covariance matrix can thus be generated as

$$(\mathbf{C}_*)_{st} = C(h_{st}), \quad s, t = 1, \ldots, \dagger, \tag{B5}$$

where the subscript ' * ' denotes either a^0 or c_i^0 which leads to ' † ' being either N_a or N_{c_i}, respectively.

The covariance matrices $\mathbf{C}_{c_1^0}$, $\mathbf{C}_{c_2^0}$, and $\mathbf{C}_{a^0}$ can be non-diagonal, to allow for anisotropic correlations. The anisotropy will be specified trough the angle, γ, from the z-axis to the principal axis corresponding to the largest eigenvalue, and the anisotropy ratio, δ. Numerical values for α, β, γ, and δ will be given in Section 4.2.

For an in-depth description of the EnKF applied to a geophysical method (CSEM) and generation of the initial ensemble with the reduced, smoothed level-set representation, with examples, see Tveit et al. (2015a).

Appendix C Sample mean and covariance matrix

Let $\mathbf{Y} = (\mathbf{y}_1, \mathbf{y}_2, \ldots, \mathbf{y}_{N_e})$ denote an arbitrary ensemble matrix, and let $\mathbf{u}$ denote an N_e-vector where all entries equal unity. The sample (empirical) mean may then be written as

$$\widetilde{\mathbf{y}} = \frac{1}{N_e}\mathbf{Y}\mathbf{u}. \tag{C1}$$

Furthermore, let $\mathbf{U} = (\mathbf{u}, \mathbf{u}, \ldots, \mathbf{u})$ (i.e. with N_e columns), and define the sample mean matrix as $\widetilde{\mathbf{Y}} = \frac{1}{N_e}\mathbf{Y}\mathbf{U}$. The sample cross-covariance matrix between two arbitrary random vectors, $\mathbf{y}$ and $\mathbf{z}$, is then given as

$$\widetilde{\mathbf{C}}_{yz} = \frac{1}{N_e - 1}(\mathbf{Y} - \widetilde{\mathbf{Y}})(\mathbf{Z} - \widetilde{\mathbf{Z}})^T. \tag{C2}$$

The sample auto-covariance matrix, $\widetilde{\mathbf{C}}_y$, is given by (C2) with $\mathbf{Z} = \mathbf{Y}$.

References

Aanonsen, S. I., Nævdal, G., Oliver, D. S., Reynolds, A. C., & Vallès, B. (2009, sep). The ensemble Kalman filter in reservoir engineering – a review. *SPE Journal*, *14*(3), 393–412.

Abubakar, A., Gao, G., Habashy, T. M., & Liu, J. (2012). Joint inversion approaches for geophysical electromagnetic and elastic full-waveform data. *Inverse Probl.*, *28*(5), 055016.

Agersborg, R., Hille, L. T., Lien, M., Lindgård, J. E., Ruiz, H., & Vatshelle, M. (2017, aug). Mapping water influx and hydrocarbon depletion in offshore reservoirs using gravimetry: Requirements on gravimeter calibration. In *Seg technical program expanded abstracts 2017* (pp. 1803–1807). Houston, USA: Society of Exploration Geophysicists.

Aki, K., & Richards, P. G. (1980). *Quantitative Seismology: Theory and Methods.* W.H. Freeman & Co.

Alnes, H., Eiken, O., Nooner, S., Sasagawa, G., Stenvold, T., & Zumberge, M. (2011). Results from Sleipner gravity monitoring: updated density and temperature distribution of the CO_2 plume. *Energy Proced.*, *4*, 5504–5511.

Appriou, D., & Bonneville, A. (2021). Monitoring carbon storage sites with time-lapse gravity surveys. In *Geophysical monitoring for geologic carbon storage.* American Geophysical Union (AGU), to appear.

Aruliah, D. A., Ascher, U. M., Haber, E., & Oldenburg, D. (2001, feb). A method for the forward modelling of 3-D electromagnetic quasi-static problems. *Math Mod. Meth. Appl. S.*, *11*(01), 1–21. doi: 10.1142/S0218202501000702

Berre, I., Lien, M., & Mannseth, T. (2009). Multi-level parameter structure identification for two-phase porous-media flow problems using flexible representations. *Adv. Water Resour.*, *32*(12), 1777–1788.

Berre, I., Lien, M., & Mannseth, T. (2011). Identification of three-dimensional electric conductivity changes from time-lapse electromagnetic observations. *J. Comput. Phys.*, *230*(10), 3915–3928.

Bhuyian, A. H., Landrø, M., & Johansen, S. E. (2012). 3D CSEM modeling and time-lapse sensitivity analysis for subsurface CO_2 storage. *Geophysics*, *77*(5), E343–E355.

Bodin, T., & Sambridge, M. (2009, sep). Seismic tomography with the reversible

jump algorithm. *Geophys. J. Int.*, *178*(3), 1411–1436.

Bøe, R., Magnus, C., Osmunden, P. T., & Rindstad, B. I. (2002). CO_2 point sources and subsurface storage capacities for CO_2 in aquifers in Norway. *NGU report*.

Buland, A., & Kolbjørnsen, O. (2012, jan). Bayesian inversion of CSEM and magnetotelluric data. *Geophysics*, *77*(1), E33–E42.

Buland, A., & Omre, H. (2003). Bayesian linearized AVO inversion. *Geophysics*, *68*(1), 185–198.

Chen, J., & Hoversten, M. G. (2012). Joint inversion of marine seismic AVA and CSEM data using statistical rock-physics models and Markov random fields. *Geophysics*, *77*(1), R65–R80.

Chilès, J.-P., & Delfiner, P. (2012). *Geostatistics, Modeling Spatial Uncertainty*. Wiley.

Chopra, S., & Castagna, J. P. (2014). *AVO*. Society of Exploration Geophysicists.

COMSOL Inc. (2013). *Introduction to COMSOL Multiphysics*. COMSOL Software.

Constable, S. (2010). Ten years of marine CSEM for hydrocarbon exploration. *Geophysics*, *75*(5), 75A67–75A81. doi: 10.1190/1.3483451

Constable, S. (2013, jun). Review paper: Instrumentation for marine magnetotelluric and controlled source electromagnetic sounding. *Geophys. Prospect.*, *61*, 505–532. doi: 10.1111/j.1365-2478.2012.01117.x

Constable, S., Kannberg, P. K., & Weitemeyer, K. (2016). Vulcan: A deep-towed csem receiver. *Geochemistry, Geophysics, Geosystems*, *17*(3), 1042-1064. doi: https://doi.org/10.1002/2015GC006174

Davolio, A., Maschio, C., & Schiozer, D. J. (2012, oct). Pressure and saturation estimation from P and S impedances: a theoretical study. *J. Geophys. Eng.*, *9*(5), 447–460.

De Stefano, M., Andreasi, F. G., Re, S., Virgilio, M., & Snyder, F. F. (2011). Multiple-domain, simultaneous joint inversion of geophysical data with application to subsalt imaging. *Geophysics*, *76*(3), R69–R80.

Dorn, O., & Villegas, R. (2008). History matching of petroleum reservoirs using a level set technique. *Inverse Probl.*, *24*(3), 035015.

Eidesmo, T., Ellingsrud, S., MacGregor, L. M., Constable, S., Sinha, M. C., Johansen, S., ... Westerdahl, H. (2002). Sea Bed Logging (SBL), a new method for remote and direct identification of hydrocarbon filled layers in deepwater areas.

First Break, *20*(3), 144–152.

Elenius, M., Skurtveit, E., Yarushina, V., Baig, I., Sundal, A., Wangen, M., ... Gasda, S. E. (2018). Assessment of co2 storage capacity based on sparse data: Skade formation. *International Journal of Greenhouse Gas Control*, *79*, 252 - 271.

Emerick, A. A., & Reynolds, A. C. (2013). Ensemble smoother with multiple data assimilation. *Comput. Geosci.*, *55*, 3–15.

Evensen, G. (1994). Sequential data assimilation with a nonlinear quasi-geostrophic model using Monte Carlo methods to forecast error statistics. *J. Geophys. Res.*, *99*(C5), 10143–10162.

Evensen, G. (2009). *Data Assimilation: The Ensemble Kalman Filter*. Springer.

Fossum, K., & Mannseth, T. (2014a). Parameter sampling capabilities of sequential and simultaneous data assimilation: I. analytical comparison. *Inverse Probl.*, *30*(11), 114002.

Fossum, K., & Mannseth, T. (2014b). Parameter sampling capabilities of sequential and simultaneous data assimilation: Ii. statistical analysis of numerical results. *Inverse Probl.*, *30*(11), 114003.

Fossum, K., & Mannseth, T. (2015). Assessment of ordered sequential data assimilation. *Computat. Geosci.*, *19*(4), 821–844.

Gallardo, L. A., & Meju, M. A. (2003). Characterization of heterogeneous near-surface materials by joint 2D inversion of dc resistivity and seismic data. *Geophys. Res. Lett.*, *30*(13).

Gallardo, L. A., & Meju, M. A. (2011, mar). Structure-coupled multiphysics imaging in geophysical sciences. *Rev. Geophys.*, *49*(1), RG1003.

Gasperikova, E., & Hoversten, G. M. (2008, nov). Gravity monitoring of CO_2 movement during sequestration: Model studies. *Geophysics*, *73*(6), WA105–WA112.

Gineste, M., & Eidsvik, J. (2015, sep). Framework for seismic inversion of full waveform data using sequential filtering. In *Petroleum geostatistics 2015.* EAGE Publications BV. doi: 10.3997/2214-4609.201413632

Gineste, M., & Eidsvik, J. (2017, jun). Seismic waveform inversion using the ensemble kalman smoother. In *79th EAGE conference and exhibition 2017.* EAGE Publications BV. doi: 10.3997/2214-4609.201700794

Grude, S., Landrø, M., & Osdal, B. (2013). Time-lapse pressure-saturation discrim-

ination for CO_2 storage at the Snøhvit field. *Int. J. Greenh. Gas. Con.*, *19*, 369–378.

Gunning, J., & Glinsky, M. E. (2004, jul). Delivery: an open-source model-based Bayesian seismic inversion program. *Comput. Geosci.*, *30*(6), 619–636.

Haber, E., & Oldenburg, D. (1997, feb). Joint inversion: a structural approach. *Inverse Probl.*, *13*(1), 63–77.

Halland, E. K., Johansen, W. T., & Riis, F. (2014). *CO_2 storage atlas Norwegian North Sea*. Norwegian Petroleum Directorate, Stavanger, Norway.

Hare, J. L., Ferguson, J. F., & Brady, J. L. (2008). The 4D microgravity method for waterflood surveillance: Part IV – Modeling and interpretation of early epoch 4D gravity surveys at Prudhoe Bay, Alaska. *Geophysics*, *73*(6), WA163–WA171.

Hohmann, G. W. (1975, apr). Three-dimensional induced polarization and electromagnetic modeling. *Geophysics*, *40*(2), 309–324. doi: 10.1190/1.1440527

Hoversten, G. M., Cassassuce, F., Gasperikova, E., Newman, G. A., Chen, J., Rubin, Y., ... Vasco, D. (2006, may). Direct reservoir parameter estimation using joint inversion of marine seismic AVA and CSEM data. *Geophysics*, *71*(3), C1–C13.

Hu, W., Abubakar, A., & Habashy, T. M. (2009). Simultaneous multifrequency inversion of full-waveform seismic data. *Geophysics*, *74*(2), R1–R14.

Ishido, T., Tosha, T., Akasaka, C., Nishi, Y., Sugihara, M., Kano, Y., & Nakanishi, S. (2011). Changes in geophysical observables caused by CO_2 injection into saline aquifers. *Energy Procedia*, *4*, 3276–3283.

Jakobsen, M., & Tveit, S. (2018, sep). Distorted Born iterative T-matrix method for inversion of CSEM data in anisotropic media. *Geophy. J. Int.*, *214*(3), 1524–1537. doi: 10.1093/gji/ggy197

Jazwinski, A. H. (1970). *Stochastic processes and filtering theory*. Academic Press.

Kalman, R. E. (1960). A new approach to linear filtering and prediction problems. *J. Basic Eng.*, *82*(1), 35–45.

Key, K. (2012, jun). Marine electromagnetic studies of seafloor resources and tectonics. *Surv. Geophys.*, *33*(1), 135–167.

Key, K. (2016). MARE2DEM: a 2-D inversion code for controlled-source electromagnetic and magnetotelluric data. *Geophys. J. Int.*, *207*(1), 571–588.

Key, K., & Ovall, J. (2011). A parallel goal-oriented adaptive finite element method for 2.5-D electromagnetic modelling. *Geophys. J. Int.*, *186*(1), 137–154.

Landrø, M. (2001). Discrimination between pressure and fluid saturation changes from time-lapse seismic data. *Geophysics*, *66*(3), 836–844.

Landrø, M., & Zumberge, M. (2017, may). Estimating saturation and density changes caused by CO 2 injection at Sleipner – Using time-lapse seismic amplitude-variation-with-offset and time-lapse gravity. *Interpretation*, *5*(2), T243–T257.

Lang, X., & Grana, D. (2019, may). Rock physics modelling and inversion for saturation-pressure changes in time-lapse seismic studies. *Geophysical Prospecting*, *67*(7), 1912–1928. doi: 10.1111/1365-2478.12797

Li, Y., & Oldenburg, D. W. (1998, jan). 3-D inversion of gravity data. , *63*(1), 109–119.

Lien, M. (2013). Simultaneous joint inversion of amplitude-versus-offset and controlled-source electromagnetic data by implicit representation of common parameter structure. *Geophysics*, *78*(4), ID15–ID27.

Lien, M., Berre, I., & Mannseth, T. (2005). Combined adaptive multiscale and level-set parameter estimation. *Multiscale Model. Simul.*, *4*(4), 1349–1372.

Lien, M., & Mannseth, T. (2008). Sensitivity study of marine CSEM data for reservoir production monitoring. *Geophysics*, *73*(4), F151–F163.

Lines, L. R., Schultz, A. K., & Treitel, S. (1988). Cooperative inversion of geophysical data. *Geophysics*, *53*(1), 8–20.

Litman, A. (2005). Reconstruction by level sets of n-ary scattering obstacles. *Inverse Probl.*, *21*(6), S131–S152.

Liu, M., & Grana, D. (2018, apr). Stochastic nonlinear inversion of seismic data for the estimation of petroelastic properties using the ensemble smoother and data reparameterization. *Geophysics*, *83*(3), M25–M39. doi: 10.1190/geo2017-0713.1

Longxiao, Z., Hanming, G., & Yan, L. (2016). The time-lapse AVO difference inversion for changes in reservoir parameters. *J. Geophys. Eng.*, *13*(6), 899–911.

Løseth, L. O., Pedersen, H. M., Ursin, B., Amundsen, L., & Ellingsrud, S. (2006, jul). Low-frequency electromagnetic fields in applied geophysics: Waves or diffusion? *Geophysics*, *71*(4), W29–W40. doi: 10.1190/1.2208275

Mannseth, T. (2014). Relation between level set and truncated pluri-gaussian methodologies for facies representation. *Math. Geosci.*, *46*(6), 711–731.

Mavko, G., Mukerji, T., & Dvorkin, J. (2009). *The rock physics handbook*. Cam-

bridge University Press. doi: 10.1017/cbo9780511626753

Moorkamp, M., Heincke, B., Jegen, M., Roberts, A. W., & Hobbs, R. W. (2011, jan). A framework for 3-D joint inversion of MT, gravity and seismic refraction data. *Geophys. J. Int.*, *184*(1), 477–493.

Mur, A., Daley, T., & Harbert, W. (2021). Tracking subsurface co_2 using advanced reflection seismic and well log-based workflows incorporating fluid density and pore pressure effects: Relevance to reservoir monitoring and supercritical co_2 enhanced oil recovery. In *Geophysical monitoring for geologic carbon storage.* American Geophysical Union (AGU), to appear.

Nabighian, M. N. (1991). *Electromagnetic Methods in Applied Geophysics: Volume 2, Application, Parts A and B.* Society of Exploration Geophysicists. doi: 10.1190/1.9781560802686

Orange, A., Key, K., & Constable, S. (2009). The feasibility of reservoir monitoring using time-lapse marine CSEM. *Geophysics*, *74*(2), F21–F29.

Park, J., Sauvin, G., & Vöge, M. (2017). 2.5D inversion and joint interpretation of CSEM data at Sleipner CO_2 storage. *Energy Procedia*, *114*, 3989–3996.

Rafiee, J., & Reynolds, A. C. (2017, nov). Theoretical and efficient practical procedures for the generation of inflation factors for ES-MDA. *Inverse Problems*, *33*(11), 115003.

Ray, A., & Key, K. (2012, oct). Bayesian inversion of marine CSEM data with a trans-dimensional self parametrizing algorithm. *Geophys. J. Int.*, *191*(3), 1135–1151.

Schlumberger Ltd. (2009). *ECLIPSE Reservoir Simulation Software: Reference Manual*. Schlumberger Software.

Shewchuk, J. R. (1996). Triangle: engineering a 2D quality mesh generator and Delaunay triangulator. In *Applied computational geometry: Towards geometric engineering,* lecture notes in computer science, vol. 1148 (pp. 203–222). Springer.

Souza, R., Lumley, D., & Shragge, J. (2017, feb). Estimation of reservoir fluid saturation from 4D seismic data: effects of noise on seismic amplitude and impedance attributes. *J. Geophys. Eng.*, *14*(1), 51–68.

Takougang, E. M. T., Harris, B., Kepic, A., & Le, C. V. A. (2015). Cooperative joint inversion of 3D seismic and magnetotelluric data: With application in a mineral province. *Geophysics*, *80*(4), R175–R187.

Talwani, M., Worzel, J. L., & Landisman, M. (1959). Rapid gravity computations for two-dimensional bodies with application to the Mendocino submarine fracture zone. *J. Geophys. Res.*, *64*(1), 49–59.

Thurin, J., Brossier, R., & Métivier, L. (2017, jun). Ensemble-based uncertainty estimation in full waveform inversion. In *79th EAGE conference and exhibition 2017.* EAGE Publications BV. doi: 10.3997/2214-4609.201701007

Trani, M., Arts, R., Leeuwenburgh, O., & Brouwer, J. (2011). Estimation of changes in saturation and pressure from 4D seismic AVO and time-shift analysis. *Geophysics*, *76*(2), C1–C17.

Tura, A., & Lumley, D. E. (1999, jan). Estimating pressure and saturation changes time-lapse AVO data. In *Seg technical program expanded abstracts 1999* (pp. 1655–1658). Houston, USA.

Tveit, S., Bakr, S. A., Lien, M., & Mannseth, T. (2015a). Ensemble-based Bayesian inversion of CSEM data for subsurface structure identification. *Geophys. J. Int.*, *201*(3), 1849–1867.

Tveit, S., Bakr, S. A., Lien, M., & Mannseth, T. (2015b). Identification of subsurface structures using electromagnetic data and shape priors. *J. Comput. Phys.*, *284*, 505–527.

Tveit, S., Mannseth, T., & Jakobsen, M. (2016, sep). Discriminating time-lapse saturation and pressure changes in CO_2 monitoring from seismic waveform and CSEM data using ensemble-based Bayesian inversion. In *Seg technical program expanded abstracts 2016* (pp. 5485–5489). Dallas, USA.

Tveit, S., Mannseth, T., Park, J., Sauvin, G., & Agersborg, R. (2020, mar). Combining CSEM or gravity inversion with seismic AVO inversion, with application to monitoring of large-scale CO2 injection. *Computational Geosciences*. doi: 10.1007/s10596-020-09934-9

Um, E. S., & Alumbaugh, D. L. (2007). On the physics of the marine controlled-source electromagnetic method. *Geophysics*, *72*(2), WA13–WA26. doi: 10.1190/1.2432482

Um, E. S., Commer, M., & Newman, G. A. (2014). A strategy for coupled 3D imaging of large-scale seismic and electromagnetic data sets: Application to subsalt imaging. *Geophysics*, *79*(3), ID1–ID13.

van Leeuwen, P. J., & Evensen, G. (1996). Data assimilation and inverse methods in

terms of a probabilistic formulation. *Mon. Weather Rev.*, *124*(12), 2898–2913.

Vatshelle, M., Glegola, M., Lien, M., Noble, T., & Ruiz, H. (2017, jun). Monitoring the Ormen Lange Field with 4D Gravity and Seafloor Subsidence. In *79th eage conference and exhibition.* Paris, France.

Vese, L. A., & Chan, T. F. (2002). A multiphase level set framework for image segmentation using the Mumford and Shah model. *Int. J. Comput. Vision*, *50*(3), 271–293.

Wannamaker, P. E., Hohmann, G. W., & SanFilipo, W. A. (1984, jan). Electromagnetic modeling of three dimensional bodies in layered earths using integral equations. *Geophysics*, *49*(1), 60–74. doi: 10.1190/1.1441562

Weidelt, P. (2007, oct). Guided waves in marine CSEM. *Geophysical Journal International*, *171*(1), 153–176. doi: 10.1111/j.1365-246X.2007.03527.x

Yee, K. S. (1966, may). Numerical solution of initial boundary value problems involving Maxwell's equations in isotropic media. *IEEE T. Antenn. Propag.*, *14*(3), 302–307. doi: 10.1109/TAP.1966.1138693

Zumberge, M., Alnes, H., Eiken, O., Sasagawa, G., & Stenvold, T. (2008). Precision of seafloor gravity and pressure measurements for reservoir monitoring. *Geophysics*, *73*(6), WA133–WA141.